Mon. Not. R. Astron. Soc. **392,** 52–76 (2009) doi:10.1111/j.1365-2966.2008.14056.x

Relativistic simulations of the phase-transition-induced collapse of neutron stars

Ernazar B. Abdikamalov,[1,2⋆] Harald Dimmelmeier,[3,4] Luciano Rezzolla[5,6,7] and John C. Miller[1,8]

[1] *International School of Advanced Studies (SISSA) and INFN, Via Beirut 2–4, I-34014 Trieste, Italy*
[2] *Institute of Nuclear Physics, Uzbekistan Academy of Sciences, Ulughbek, Uzbekistan*
[3] *Department of Physics, Aristotle University of Thessaloniki, GR-54124 Thessaloniki, Greece*
[4] *Max-Planck-Institut für Astrophysik, Karl-Schwarzschild-Strasse 1, D-85741 Garching, Germany*
[5] *Max-Planck-Institut für Gravitationsphysik, Albert-Einstein-Institut, Am Mühlenberg 1, D-14476 Golm, Germany*
[6] *Department of Physics and Astronomy, Louisiana State University, Baton Rouge, LA 70803, USA*
[7] *INFN, Department of Physics, University of Trieste, Trieste, Italy*
[8] *Department of Physics (Astrophysics), University of Oxford, Keble Road, Oxford OX1 3RH*

Accepted 2008 October 8. Received 2008 September 16; in original form 2008 June 10

ABSTRACT

An increase in the central density of a neutron star may trigger a phase transition from hadronic matter to deconfined quark matter in the core, causing it to collapse to a more compact hybrid star configuration. We present a study of this, building on previous work by Lin et al.. We follow them in considering a supersonic phase transition and using a simplified equation of state, but our calculations are general relativistic (using 2D simulations in the conformally flat approximation) as compared with their 3D Newtonian treatment. We also improved the treatment of the initial phase transformation, avoiding the introduction of artificial convection. As before, we find that the emitted gravitational wave spectrum is dominated by the fundamental quasi-radial and quadrupolar pulsation modes but the strain amplitudes are much smaller than suggested previously, which is disappointing for the detection prospects. However, we see significantly smaller damping and observe a non-linear mode resonance which substantially enhances the emission in some cases. We explain the damping mechanisms operating, giving a different view from the previous work. Finally, we discuss the detectability of the gravitational waves, showing that the signal-to-noise ratio for current or second generation interferometers could be high enough to detect such events in our Galaxy, although third generation detectors would be needed to observe them out to the Virgo cluster, which would be necessary for having a reasonable event rate.

Key words: hydrodynamics – relativity – methods: numerical – stars: neutron – stars: oscillations – stars: rotation.

1 INTRODUCTION

The existence of compact stellar objects partially or totally consisting of matter in a deconfined quark phase was already predicted long ago (Itoh 1970; Bodmer 1971; Witten 1984). Such stars are thought likely to originate as a result of the conversion of purely hadronic matter in the interior of a neutron star (NS) into a deconfined quark matter phase when the density exceeds a certain threshold (for a review, see e.g. Weber 1999; Glendenning 2002). We focus here on cases where the conversion occurs only in the core of the NS, while the outer parts remain unchanged. The theory of dense nuclear matter predicts that such compact stars [hereafter we will use the term 'hybrid quark star' (HQS) when referring to these objects] would generally be more compact than the progenitor standard NS, and their equilibrium radii would be smaller by up to 20 per cent. The potential energy W released by the phase transition is expected to be of the order of

$$\Delta W \sim \frac{M^2}{R}\frac{\Delta R}{R} \sim 10^{52}\ \mathrm{erg},$$

where R and M are the typical radius and mass of the NS, respectively, and ΔR is the decrease in radius.

A first-order phase transition is expected to be the most interesting case as far as the dynamics and structure of the star are concerned. Such a transition would proceed by the conversion of initially metastable hadronic matter in the core into the new deconfined quark phase (Zdunik et al. 2007, 2008). The metastable phase could be formed as the central density of the NS increases

⋆E-mail: abdik@sissa.it

due to mass accretion, spin-down or cooling. This could happen soon after the birth of the NS in a supernova or it could occur for an old NS accreting from a binary companion. The first of these channels is likely to give the higher event rate but the second is also interesting. In the widely accepted scenario for the formation of millisecond pulsars, where an old NS is spun up by accretion from a binary companion, the amount of spin-up would be directly related to the amount of mass accreted (Burderi et al. 1999), meaning that there would be a population of rapidly rotating NSs with rather high mass (and hence high central densities). Recent observational data seem to confirm that a significant proportion of millisecond pulsars do indeed tend to be high-mass objects (Freire et al. 2008) which would then be candidates for undergoing (or having undergone) a phase-transition-induced collapse of the type which we are discussing here. While some significant proportion of the potential energy release given by equation (1) would probably go into neutrino emission, a significant proportion might also go into pulsations of the newly formed HQS, if the conversion process to the new phase is rapid enough, and this could be an interesting source of gravitational waves (GWs; see Marranghello et al. 2002; Miniutti et al. 2003; Lin et al. 2006). If detected, these GW signals, and in particular the identification of quasi-normal mode frequencies in their spectrum, could help to constrain the properties of matter at the high densities encountered here. For non-rotating cold NSs with various compositions, the related theory of asteroseismology has already been formulated in recent years (Andersson & Kokkotas 1998; Kokkotas, Apostolatos & Andersson 2001; Benhar, Ferrari & Gualtieri 2004).

A problem for making any detailed studies of phase-transition-induced collapse is that the description of the physics of the phase transition remains very uncertain and controversial (for a recent review see Horvath 2007). Drago, Lavagno & Parenti (2007) discussed possible modes of burning of hadronic matter into quark matter in the framework of relativistic hydrodynamics using a microphysical equation of state (EOS). They found that the conversion process always corresponds to a deflagration and never to a detonation. They also argued that hydrodynamical instabilities can develop at the burning front. They estimated the corresponding increase in the propagation velocity of the phase transition and noted that, although the increase is significant, it is not sufficient to transform the deflagration into a detonation in essentially all realistic scenarios. On the other hand, Bhattacharyya et al. (2006) considered the transition as being a two-step process, in which the hadronic matter is first converted to two-flavour u and d quark matter, which then subsequently transforms into strange quark matter (u, d and s quarks) in a second step. They used the relativistic hydrodynamic equations to calculate the propagation velocity of the first front and found that, in this first stage, a detonation wave develops in the hadronic matter. After this front passes through, leaving behind two-flavour matter, a second front is generated which transforms the two-flavour matter to three-flavour matter via weak interactions. The time-scale for the second conversion is $\sim$100 s, while that for the first step is about 1 ms.

Against this background, Lin et al. (2006; hereafter referred to as LCCS) carried out a first study of GW emission by a phase-transition-induced collapse of a rotating NS to an HQS, using a very simplified model for the microphysics and treating the phase transition as occurring instantaneously. On the basis of 3D calculations using Newtonian gravity and hydrodynamics, they obtained waveforms of the emitted GWs for several collapse models, and found that the typical predicted dimensionless GW strain h ranged from 3 to 15 $\times$ 10^{-23} for a source at a distance of 10 Mpc. The corresponding energy $E_{\rm gw}$ carried away by the GWs was found to be between 0.3 and 2.8 $\times$ 10^{51} erg. They also determined the modes of stellar pulsation excited by the collapse and showed that the spectrum of the emitted GWs was dominated by the fundamental quasi-radial and quadrupolar pulsation modes of the final star. They suggested that the damping of the stellar pulsations observed in their calculations was due to the production of shock waves leading to the development of differential rotation, which proceeds on a time-scale of about 5 ms for typical collapse models.

The study by LCCS treated the conversion process as being instantaneous, and this was mimicked by replacing, at the initial time, the EOS describing the hadronic nuclear matter in the core (with which the initial equilibrium model had been built) by one describing a central zone of deconfined quarks surrounded by a region of mixed phase. The material outward of this remained in the original hadronic phase. In a first-order phase transition that proceeds via a detonation, the conversion front propagates supersonically with respect to the matter ahead of it. The sound speed in the stellar interior typically has a value of the order of 0.3–0.5c. Assuming that the quark matter core has a radius of about $R \sim 5$ km, a rough estimate for the time-scale of a supersonic conversion gives $\tau \sim R/v \sim 0.05$ ms. Clearly, this value is not much smaller than the dynamical time-scale of an NS and so one does not know, a priori, the impact that the properties of the conversion would have for the subsequent stellar dynamics taking place on similar time-scales. Therefore, one should first check how the dynamics of the star after the phase transition would depend on the finite propagation velocity of the front, and we do this here.

LCCS represented the hadronic matter by means of a polytropic EOS, initially having an adiabatic index $\gamma = 2$. When the phase transition was triggered (by changing the EOS in the central regions, reducing the pressure support), they also replaced the original hadronic EOS by a softer ideal gas type of EOS (with γ then ranging from 1.95 to 1.75 depending on the model), which artificially lowered the pressure *outside* the deconfined quark matter core as well (see their equation 44). The lowering of the adiabatic index also in the outer regions leads to an increased release of gravitational binding energy and is hard to motivate on physical grounds.

Although the study by LCCS was an important step forward, it was clearly using an extremely simplified model for the physics of the NS matter and of the phase transition (as well as not including emission processes other than GW emission) and one must question how closely it represents such processes occurring in real NSs. Since the full problem is complex and involves some input physics which is very incompletely known at present, the only way to make progress at this stage is, indeed, to work in terms of simplified models but making improvements where possible. The strategy of this paper is to take the work of LCCS as a starting point and then to take some steps forward in the direction of including further aspects. In particular, the effects of general relativity (GR) certainly play an important role in such studies: for instance, the total rest mass of a typical Newtonian NS may be almost twice as large as that of its counterpart in GR with the same central density and the same EOS. The impact of GR is even more pronounced if the star is near to the maximum mass limit. Therefore, one expects the Newtonian and GR descriptions of NS collapse to differ significantly, thus necessitating a proper treatment of the GR effects.

In this study we extend the previous work of LCCS in a number of ways: (i) we take into account the effects of GR; (ii) we modify the EOS of the stellar matter only in regions which undergo the phase transition and take care to avoid introducing spurious convection; (iii) we consider a larger set of physical models for different values

of the stellar parameters and different properties of the stellar matter; (iv) we study the effect of introducing a finite time-scale for the initial phase transformation which destabilizes the core rather than treating it as occurring instantaneously. Our model for the HQS is based on that of LCCS. The numerical hydrodynamics simulations are here performed in axisymmetry using the conformal flatness approximation to GR. While our model remains extremely simplified, we believe that these modifications do represent valid and significant steps forward. We feel, however, that we should caution against making further elaborate extensions of the hydrodynamics (e.g. to 3D GR hydrodynamics or GR magnetohydrodynamics) until such time as one has the possibility of including a greatly improved treatment of the microphysics and emission processes so that the models come closer to those of real NSs.

This article is organized as follows. In Section 2 we summarize the numerical methods used, while in Section 3 we introduce the models investigated. In Section 4 we validate our code by performing a comparison with the Newtonian models of LCCS. In Section 5 we discuss the results of our simulations of GR models and their dependence on the various parameters, and in Section 6 we conclude with a summary. In Appendix A we examine the impact on the collapse dynamics of considering a finite time-scale for the initial phase transformation, and in Appendix B we present our method for determining the damping times for the emitted gravitational radiation waveforms.

Unless otherwise noted, we choose geometrical units for all physical quantities by setting the speed of light and the gravitational constant to one, $c = G = 1$. Latin indices run from 1 to 3, Greek indices from 0 to 3.

2 NUMERICAL METHODS

We construct our initial rotating NS equilibrium models using a variant of the self-consistent field method described by Komatsu, Eriguchi & Hachisu (1989a) (KEH hereafter), as implemented in the code RNS (Stergioulas & Friedman 1995). This code solves the GR hydrostationary equations for rotating matter distributions whose pressure obeys an EOS given by a polytropic relation (see equation 11 below). The resulting equilibrium models, which we choose to be rotating uniformly, are taken as initial data for the evolution code.

The time-dependent numerical simulations were performed with the COCONUT code developed by Dimmelmeier, Font & Müller (2002a,b) with a metric solver based on spectral methods as described in Dimmelmeier et al. (2005). The code solves the GR field equations for a curved space–time in the 3 + 1 split under the assumption of the conformal flatness condition (CFC) for the three-metric. The hydrodynamics equations are formulated in conservation form, and are evolved with high-resolution shock-capturing schemes.

In the following subsections, we summarize the mathematical formulation of the metric and hydrodynamic equations, and the numerical methods used for solving them.

2.1 Metric equations

We adopt the ADM 3 + 1 formalism of Arnowitt, Deser & Misner (1962) to foliate a space–time endowed with a four-metric $g_{\mu\nu}$ into a set of non-intersecting space-like hypersurfaces. The line element is then given by

$$ds^2 = g_{\mu\nu}\,dx^\mu dx^\nu = -\alpha^2\,dt^2 + \gamma_{ij}(dx^i + \beta^i\,dt)(dx^j + \beta^j\,dt), \quad (1)$$

where α is the lapse function, β^i is the space-like shift three-vector and γ_{ij} is the spatial three-metric.

In the 3 + 1 formalism, the Einstein equations are split into evolution equations for the three-metric γ_{ij} and the extrinsic curvature K_{ij}, and constraint equations (the Hamiltonian and momentum constraints) which must be fulfilled at every space-like hypersurface.

The fluid is generally specified by means of the rest-mass density ρ, the four-velocity u^μ, and the pressure P, with the specific enthalpy defined as $h = 1 + \epsilon + P/\rho$, where ϵ is the specific internal energy. The three-velocity of the fluid as measured by an Eulerian observer is given by $v^i = u^i/(\alpha\,u^0) + \beta^i/\alpha$, and the Lorentz factor $W = \alpha u^0$ satisfies the relation $W = 1/\sqrt{1 - v_i v^i}$.

Based on the ideas of Isenberg (1978) and Wilson, Mathews & Marronetti (1996), and as done in the work of Dimmelmeier et al. (2002a,b), we approximate the general metric $g_{\mu\nu}$ by replacing the spatial three-metric γ_{ij} with the conformally flat three-metric

$$\gamma_{ij} = \phi^4 \hat{\gamma}_{ij}, \quad (2)$$

where $\hat{\gamma}_{ij}$ is the flat metric and ϕ is a conformal factor. In this CFC approximation, the ADM equations for the space–time metric reduce to a set of five coupled elliptic non-linear equations for the metric components,

$$\begin{aligned}
\hat{\Delta}\phi &= -2\pi\phi^5\left(\rho h W^2 - P\right) - \phi^5\frac{K_{ij}K^{ij}}{8},\\
\hat{\Delta}(\alpha\phi) &= 2\pi\alpha\phi^5\left[\rho h(3W^2 - 2) + 5P\right] + \alpha\phi^5\frac{7K_{ij}K^{ij}}{8},\\
\hat{\Delta}\beta^i &= 16\pi\alpha\phi^4\rho h W^2 v^i + 2\phi^{10}K^{ij}\hat{\nabla}_j\left(\alpha\phi^{-6}\right) - \frac{1}{3}\hat{\nabla}^i\hat{\nabla}_k\beta^k, \quad (3)
\end{aligned}$$

where the maximal slicing condition, $K^i_i = 0$, is imposed. Here $\hat{\nabla}_i$ and $\hat{\Delta}$ are the flat space Nabla and Laplace operators, respectively. For the extrinsic curvature we have the expression

$$K_{ij} = \frac{1}{2\alpha}\left(\nabla_i\beta_j + \nabla_j\beta_i - \frac{2}{3}\gamma_{ij}\nabla_k\beta^k\right), \quad (4)$$

which closes system (3).

We rewrite the above metric equations in a mathematically equivalent form by introducing an auxiliary vector field W^i and obtain

$$\begin{aligned}
\hat{\Delta}\phi &= -2\pi\phi^5\left(\rho h W^2 - P\right) - \phi^{-7}\frac{\hat{K}_{ij}\hat{K}^{ij}}{8},\\
\hat{\Delta}(\alpha\phi) &= 2\pi\alpha\phi^5\left[\rho h(3W^2 - 2) + 5P\right] + \alpha\phi^{-7}\frac{7\hat{K}_{ij}\hat{K}^{ij}}{8},\\
\hat{\Delta}\beta^i &= 2\hat{\nabla}_j\left(2\alpha\phi^{-6}\hat{K}^{ij}\right) - \frac{1}{3}\hat{\nabla}^i\hat{\nabla}_k\beta^k,\\
\hat{\Delta}W^i &= 8\pi\phi^{10}\rho h W^2 v^i - \frac{1}{3}\hat{\nabla}^i\hat{\nabla}_k W^k, \quad (5)
\end{aligned}$$

where the flat space extrinsic curvature is given by

$$\hat{K}_{ij} = \hat{\nabla}_i W_j + \hat{\nabla}_j W_i - \frac{2}{3}\hat{\gamma}_{ij}\hat{\nabla}_k W^k \quad (6)$$

and relates to the regular extrinsic curvature as $\hat{K}_{ij} = \phi^2 K_{ij}$ and $\hat{K}^{ij} = \phi^{10}K^{ij}$. The advantages of this new formulation of the metric equations will be discussed in a future publication.

Note that the metric equations do not contain explicit time derivatives, and thus the metric is calculated by a fully constrained approach, at the cost of neglecting some evolutionary degrees of freedom in the space–time metric (e.g. dynamical GW degrees of freedom).

The accuracy of the CFC approximation for isolated compact stellar objects has been tested in various works, both in the context

of stellar core collapse and for equilibrium models of NSs (for a detailed comparison between the CFC approximation of GR and full GR, see Ott et al. 2007, and references therein). In particular, Dimmelmeier et al. (2006b) compared collapse simulations of rotating massive stellar cores in the CFC approximation with the full GR calculations of Shibata & Sekiguchi (2005). Although such massive stellar cores are rather unmotivated astrophysically, they are nice toy models where the space–time dynamics during collapse is violent, similar to what is expected in the case of the collapse of NSs to HQSs. For example, some models almost collapse to black holes, with the value of the lapse function reaching 0.29. The comparison by Dimmelmeier et al. (2006b) reveals very good agreement between the CFC and full GR calculations. We thus conclude that the space–time of rapidly rotating NS models (whether uniformly or differentially rotating) is still very well approximated by the CFC metric (2). The accuracy of the approximation is expected to degrade only in extreme cases, such as a rapidly rotating black hole, a self-gravitating thin disc or a compact binary system.

2.2 General relativistic hydrodynamics

The hydrodynamic evolution of a standard relativistic perfect fluid is determined by the local conservation equations

$$\nabla_\mu J^\mu = 0, \qquad \nabla_\mu T^{\mu\nu} = 0, \tag{7}$$

where $J^\mu = \rho u^\mu$ is the rest-mass current, and ∇_μ denotes the covariant derivative with respect to the four-metric $g_{\mu\nu}$. Following Banyuls et al. (1997), we introduce a set of conserved variables in terms of the primitive (physical) variables (ρ, v_i, ϵ):

$$D = \rho W, \qquad S_i = \rho h W^2 v_i, \qquad \tau = \rho h W^2 - P - D.$$

Using these, the local conservation laws (7) can be written as a first-order, flux-conservative hyperbolic system of equations,

$$\frac{\partial \sqrt{\gamma}\boldsymbol{U}}{\partial t} + \frac{\partial \sqrt{-g}\boldsymbol{F}^i}{\partial x^i} = \sqrt{-g}\boldsymbol{S}, \tag{8}$$

with the state vector, flux vector and source vector being

$$\begin{aligned}
\boldsymbol{U} &= [D, S_j, \tau], \\
\boldsymbol{F}^i &= \left[D\hat{v}^i, S_j\hat{v}^i + \delta^i_j P, \tau\hat{v}^i + Pv^i\right], \\
\boldsymbol{S} &= \left[0, \frac{1}{2}T^{\mu\nu}\frac{\partial g_{\mu\nu}}{\partial x^j}, T^{00}\left(K_{ij}\beta^i\beta^j - \beta^j\frac{\partial\alpha}{\partial x^j}\right)\right. \\
&\quad \left. + T^{0j}\left(2K_{ij}\beta^i - \frac{\partial\alpha}{\partial x^j}\right) + T^{ij}K_{ij}\right],
\end{aligned} \tag{9}$$

respectively.[1] Here $\hat{v}^i = v^i - \beta^i/\alpha$, and $\sqrt{-g} = \alpha\sqrt{\gamma}$, with $g = \det(g_{\mu\nu})$ and $\gamma = \det(\gamma_{ij})$; the $\Gamma^\lambda_{\mu\nu}$ are the Christoffel symbols associated with $g_{\mu\nu}$.

The system of hydrodynamic equations (8) is closed by an EOS, which relates the pressure to some thermodynamically independent quantities; in our case $P = P(\rho, \epsilon)$.

2.3 Numerical methods for solving the metric and hydrodynamics equations

The hydrodynamic solver performs the numerical time integration of the system of conservation equations (8) using a high-resolution shock-capturing (HRSC) scheme on a finite-difference grid. In (upwind) HRSC methods, a Riemann problem has to be solved at each cell interface, which requires the reconstruction of the primitive variables (ρ, v^i, ϵ) at these interfaces. We use the PPM method for making the reconstruction, which yields third-order accuracy in space for smooth flows and away from extrema. The numerical fluxes are computed by means of Marquina's approximate flux formula (Donat et al. 1998). The time update of the state vector $\boldsymbol{U}$ is done using the method of lines in combination with a Runge–Kutta scheme having second-order accuracy in time. Once the state vector has been updated in time, the primitive variables are recovered using an iterative Newton–Raphson method. To numerically solve the elliptic CFC metric equations (3) we utilize an iterative nonlinear solver based on spectral methods. The combination of HRSC methods for the hydrodynamics and spectral methods for the metric equations within a multidimensional numerical code has been presented in detail in Dimmelmeier et al. (2005).

The COCONUT code uses Eulerian spherical polar coordinates $\{r, \theta\}$; for the models discussed in this paper we are assuming axisymmetry with respect to the rotation axis and also equatorial symmetry. The finite-difference grid consists of 200 radial grid points and 40 angular grid points, which are equidistantly spaced. A small part of the grid, which initially corresponds to 60 radial grid points, covers an artificial low-density atmosphere, extending beyond the stellar surface, whose rest-mass density is 10^{-17} of the initial central rest-mass density of the NS.

Since the calculation of the space–time metric is computationally expensive, it is updated only once every 25 hydrodynamic time-steps during the evolution and is extrapolated in between. The suitability of this procedure has been tested and discussed in detail in Dimmelmeier et al. (2002a). We also note that tests with different grid resolutions were performed to check that the regular grid resolution specified above is appropriate for our simulations. A check on the relative violation in the conservation of total rest mass, ADM mass and total angular momentum showed that each of these quantities is conserved to within 1 per cent during the entire evolution time.

2.4 Gravitational waves

The GWs emitted by the collapsing NS are computed using the Newtonian quadrupole formula in its first time-integrated form (the first-moment of momentum density formulation as described in detail in Dimmelmeier et al. 2002b) in the variant of Shibata & Sekiguchi (2004). This yields the quadrupole wave amplitude $A^{\rm E2}_{20}$ as the lowest order term in a multipole expansion of the radiation field into pure-spin tensor harmonics (Thorne 1980). The wave amplitude is related to the dimensionless GW strain h in the equatorial plane by (Dimmelmeier et al. 2002b)

$$h = \frac{1}{8}\sqrt{\frac{15}{\pi}}\frac{A^{\rm E2}_{20}}{r} = 8.8524\times10^{-21}\left(\frac{A^{\rm E2}_{20}}{10^3\,\mathrm{cm}}\right)\left(\frac{10\,\mathrm{kpc}}{r}\right), \tag{10}$$

where r is the distance from the emitting source.

We point out that although the quadrupole formula is not gauge invariant and is only strictly valid in the Newtonian slow-motion limit, for GWs emitted by pulsations of rotating NSs it gives results that agree very well in phase and to about 10–20 per cent in amplitude with more sophisticated methods (Shibata & Sekiguchi 2003; Nagar et al. 2007).

[1] Note that here we use an analytically equivalent reformulation of the energy source term as compared with the one presented in e.g. Dimmelmeier et al. (2002a).

3 STELLAR MODELS AND TREATMENT OF THE PHASE TRANSITION

3.1 Initial neutron star model

Following LCCS, we compute the initial equilibrium NS model before the phase transition using a polytropic EOS,

$$P = K\rho^{\gamma}, \tag{11}$$

where K and γ are constants. We choose $\gamma = 2$ and $K = 100$ (in units where $M_{\odot} = 1$) for all of the GR initial models considered in the present study. On the initial time-slice, we also need to specify the specific internal energy ϵ. For a polytropic EOS, the thermodynamically consistent ϵ is given by

$$\epsilon = \frac{K}{\gamma - 1}\rho^{\gamma-1}. \tag{12}$$

3.2 Hybrid quark star model

Due to the complexity of the fundamental theory of strong interactions, all theoretical studies of quark matter in compact stars are based on phenomenological models. The MIT bag model EOS, which has been used extensively for this (for a review, see e.g. Weber 1999; Glendenning 2002), is based on the following assumptions: (i) quarks appear in colour neutral clusters confined to a finite region of space, the volume of which is limited by the negative pressure of the QCD vacuum; (ii) within this region, interactions between the quarks are weak and can be treated using low-order perturbation theory in the coupling constant. These two assumptions allow the two main features of QCD to be modelled, namely colour confinement and asymptotic freedom. The parameters of the bag model are the bag constant B, the masses of the quarks and the running coupling constant α_s, whose value at the scale relevant for typical quark chemical potentials is $\alpha_s \in [0.4, 0.6]$ (Benhar et al. 2007).

At the moment there is no general consensus about the value of B. Fits to the spectrum of light hadrons give $B^{1/4} \approx 145\,\mathrm{MeV}$ (DeGrand et al. 1975), while the adjustment of B with hadronic structure functions suggests $B^{1/4} \sim 170\,\mathrm{MeV}$ (Steffens, Holtmann & Thomas 1995). On the other hand, lattice QCD calculations predict values up to $B^{1/4} \sim 190\,\mathrm{MeV}$ (Satz 1982). Hereafter, and following LCCS, we take $B^{1/4} = 170\,\mathrm{MeV}$.

The masses of the u and d quarks are of the order of a few MeV (Hagiwara et al. 2002) and can therefore be mostly neglected, whereas the mass of the s quark is much larger, its value being in the range $m_s \in [80, 155]\,\mathrm{MeV}$. Nevertheless, including this mass for the s quark, rather than taking it to be massless, would decrease the pressure by only a few per cent (Alcock & Olinto 1988). We do not expect that this would change our results qualitatively, and so we neglect it in our study. We also neglect the residual interaction between the quarks and approximate their temperature as being zero. The EOS of the MIT bag model for massless and non-interacting quarks at zero temperature is given by

$$P_q = \frac{1}{3}(e - 4B), \tag{13}$$

where e is the total energy density.

A fundamental problem appears to arise in using the hydrodynamic equations of Section 2 to describe the quark medium since the quarks are being treated as having zero rest mass. The quantity e represents only the internal energy density of the quarks and contains no rest-mass contribution. Rest mass appears as a fluid quantity, within this picture, only when the quarks become confined. Nevertheless, the continuity equation (the first equation of the system of the hydrodynamic equations 8) remains well defined if thought of in terms of baryon number (which *is* defined for the quark medium) rather than in terms of rest mass. In order to have a unified treatment for the quark matter and the hadronic matter (which is necessary since we have transformation between the two), one can define a quantity $\rho = n_b m_b$ in the quark medium (where n_b is the baryon number density and m_b is the rest mass per baryon in the hadronic medium) and then formally split the internal energy density of the quark medium into two parts, writing $e = \rho + \rho\epsilon$ as usual but bearing in mind that the first term on the right-hand side represents just a part of the internal energy density in the quark phase. If one does this, it is easy to show that the treatment of the hydrodynamics goes through unchanged in a consistent way, using this ρ and ϵ.

For the normal hadron matter, during the evolution we use an ideal gas type of EOS

$$P_h = (\gamma - 1)\rho\epsilon. \tag{14}$$

However, in contrast to LCCS, we do not reduce the adiabatic index γ from its initial value of 2, because we see no physical mechanism which could be responsible for a global reduction of pressure in the *hadronic* matter phase. Consequently, in our GR models the collapse is caused solely by the pressure change due to the introduction of *quark* matter in the core of the NS.

As first shown by Glendenning (1991, 1992), if the surface tension between the phases is not too large, relaxing the condition of local electrical neutrality would allow for the possibility of having coexistence between the two phases within a certain range of densities. In a region where this applied, one would then have many intermixed microscopic zones of the lower density hadronic matter and of the higher density quark matter. Each zone would have a net electric charge but with the mixture being electrically neutral on average and with the volume fraction occupied by the higher density phase growing from 0 at the lower density boundary of the mixed phase ρ_{hm} up to 1 at the upper-density boundary ρ_{qm}.

The value of the lower threshold density ρ_{hm}, above which free quarks start to appear, is rather uncertain. From simple geometrical considerations, nucleons should begin to touch at $\rho \sim (4\pi r_{nuc}^2/3)$, which for the characteristic nucleon radius $r_{nuc} \sim 1\,\mathrm{fm}$ gives a few times nuclear saturation density, $\rho_{nuc} = 2.7 \times 10^{14}\,\mathrm{g\,cm^{-3}}$ (Glendenning 1989). For densities above this, one expects that the boundaries of particles like p, n, Σ^-, Λ and K^- would dissolve and that quarks would start to populate free states outside the hadrons (Weber 1999). The value of the upper threshold density ρ_{qm}, marking the boundary between the mixed phase and the pure deconfined quark matter phase, is also uncertain (and is model dependent) but it is very probably in the range 4–$10\rho_{nuc}$.

According to this picture, a hybrid star would then be composed of either two or three parts: (i) a *pure hadronic* matter phase for $\rho < \rho_{hm}$, (ii) a *mixed* phase of the confined–deconfined matter for $\rho_{hm} < \rho < \rho_{qm}$ and (iii) a *pure quark* matter phase for $\rho > \rho_{qm}$ (this might or might not be present in practice, depending on the maximum density reached).

In this paper, we follow LCCS in adopting the picture outlined above and we also follow their prescription in formulating the EOS for the HQS matter:

$$P = \begin{cases} P_h & \text{for } \rho < \rho_{hm}, \\ \alpha P_q + (1-\alpha)P_h & \text{for } \rho_{hm} \le \rho \le \rho_{qm}, \\ P_q & \text{for } \rho_{qm} < \rho, \end{cases} \tag{15}$$

where

$$\alpha = 1 - \left(\frac{\rho_{\rm qm} - \rho}{\rho_{\rm qm} - \rho_{\rm hm}} \right)^{\delta} \tag{16}$$

is a factor quantifying the contribution of each of the components of the mixed phase to the total pressure. As stated above, we take $P_{\rm q}$ to be given by the MIT bag model (13), while $P_{\rm h}$ is calculated using the ideal gas EOS (14). The parameter δ is introduced in order to control the quark matter contribution to the pressure in the mixed phase: with larger δ, the contribution from $P_{\rm q}$ increases. For $\delta = 1$ we recover the EOS of LCCS. We again emphasize that, in contrast to LCCS, we do not reduce the effective adiabatic index of the nuclear matter in our GR models, but rather keep it at its initial value $\gamma = 2$ during the evolution.

For our GR models we define the transition density $\rho_{\rm hm}$ from the pure hadronic matter phase to the mixed phase to be where $P_{\rm q}$ vanishes, similarly to LCCS (although they were identifying energy density and rest-mass density within their Newtonian regime). This corresponds to $\rho_{\rm hm} = 6.97 \times 10^{14}\,{\rm g\,cm^{-3}} = 2.58\rho_{\rm nuc}$ for $B^{1/4} = 170\,{\rm MeV}$ and $\rho_{\rm nuc} = 2.7 \times 10^{14}\,{\rm g\,cm^{-3}}$. Following LCCS, we set $\rho_{\rm qm} = 9\,\rho_{\rm nuc}$ in our simulations (corresponding to $24.3 \times 10^{14}\,{\rm g\,cm^{-3}}$ for our value of $\rho_{\rm nuc}$), but this is just a rough estimate to give a working value. When we make direct comparisons with the Newtonian models of LCCS in Section 4, we use their values $\rho_{\rm hm} = 7.24 \times 10^{14}\,{\rm g\,cm^{-3}}$ and $\rho_{\rm qm} = 25.2 \times 10^{14}\,{\rm g\,cm^{-3}}$, which slightly differ from our standard values.

We want to stress that this treatment of the EOS via equations (15) and (16) is extremely rough as a representation of matter in the mixed phase experiencing the phase transition, especially when one bears in mind the behaviour of fluid elements undergoing successive compression and decompression and changing the proportions of the phases. In particular, it neglects any possible effect from local heating and from the creation and subsequent emission of neutrinos during the collapse and the subsequent bounces. However, it does have the advantage of being simple and parametrizable. By changing the values of the free parameters (e.g. δ, $\rho_{\rm hm}$ or $\rho_{\rm qm}$) it allows us to modify easily the properties of the EOS.

3.3 Parameter space

The properties of our models for the phase-transition-induced collapse depend on a number of free parameters including the initial rotation period p, the total stellar rest mass M_0, the pressure contribution of the quark component in the mixed phase (controlled by δ), etc. In order to study how the collapse dynamics depends on these quantities, we performed simulations for various sequences of models where one parameter was held fixed. For instance, in order to investigate the impact of rotation we used the models A1–A8 and B1–B6 (see Table 1). The models of sequence A have a fixed central rest-mass density $\rho_{\rm c,i} = 11.25 \times 10^{15}\,{\rm g\,cm^{-3}}$ and a varying rotation period in the range from $p = 1.00$ to 6.18 ms. The ones of sequence B have a fixed rest mass $M_0 = 1.75\,{\rm M}_\odot$ and rotation periods from $p = 1.30$ to 2.89 ms. The consequences of a variation in the rest mass of the initial NS are explored in the sequence of models C1–C4, where the rotation period is held fixed at $p = 1.80$ ms and the rest mass takes values from $M_0 = 1.65$ to $1.80\,{\rm M}_\odot$.

These initial models were then evolved as sequences CA, CB and CC with fixed EOS parameters, choosing $\delta = 2$ in each case. For the CD sequence, however, we used different values for δ (from 1 to 5) in order to assess how varying the quark contribution to the EOS in the mixed phase influences the dynamics. In this sequence, the models CD1–CD5 use the initial model A2, while CD6–CD9 are based on the initial model A5.

Table 1. Summary of the set of initial models: p is the rotation period of the NS, M_0 is the total rest mass, M is the gravitational mass, T is the rotational mass energy, W is the gravitational binding energy, $\rho_{\rm c,i}$ is the central rest-mass density and $r_{\rm e}/r_{\rm p}$ is the ratio of the equatorial and polar radii. Note that the initial models A5, B4 and C3 are identical. Model N is one of the Newtonian initial models used by LCCS.

Model	p (ms)	M_0 ($\rm M_\odot$)	M ($\rm M_\odot$)	$\rho_{\rm c,i}$ ($10^{14}\,{\rm g\,cm^{-3}}$)	$r_{\rm e}/r_{\rm p}$	$T/\lvert W\rvert$ (per cent)
A1	1.00	1.98	1.81	11.25	0.635	8.44
A2	1.20	1.85	1.70	11.25	0.785	5.30
A3	1.40	1.80	1.65	11.25	0.847	3.75
A4	1.60	1.77	1.62	11.25	0.885	2.80
A5	1.80	1.75	1.60	11.25	0.910	2.18
A6	2.00	1.73	1.59	11.25	0.928	1.74
A7	2.99	1.70	1.57	11.25	0.968	0.76
A8	5.98	1.69	1.55	11.25	0.992	0.50
B1	1.30	1.75	1.62	8.42	0.746	6.32
B2	1.40	1.75	1.61	9.48	0.815	4.57
B3	1.60	1.75	1.61	10.63	0.878	2.98
B4	1.80	1.75	1.60	11.25	0.910	2.18
B5	2.00	1.75	1.60	11.80	0.931	1.66
B6	2.98	1.75	1.60	12.86	0.972	0.66
C1	1.80	1.65	1.53	8.74	0.882	2.89
C2	1.80	1.70	1.57	9.88	0.897	2.51
C3	1.80	1.75	1.60	11.25	0.910	2.18
C4	1.80	1.80	1.65	13.70	0.927	1.75
N	1.20	2.20	1.89	9.34	0.695	7.71

In addition, in order to validate our code and to discuss the results obtained by LCCS in more detail, we simulated some of their models with a Newtonian version of the COCONUT code. Our Newtonian models CN1, CN2 and CN3 (all based on the equilibrium model N) are identical to their models G1.95, R and G1.75, with the adiabatic index γ of the EOS being reduced everywhere as they had done. For these models we used exactly the same EOS as in LCCS, which differs from our regular EOS in various ways (see Section 3.2). The models labelled $\rm CN_{nipr}$ and $\rm CN_{ipr}$ are Newtonian test models whose properties are discussed in detail in Section 4.2.

In Table 2 we list important quantities obtained in the simulations of the collapse models which are discussed in the following sections. Note that the total evolution time for all models is $t_{\rm f} = 50$ ms. At that point we simply terminate the evolution, which however could be extended to much longer times given the long-term stability of our code.

4 COMPARISON WITH NEWTONIAN MODELS

Before discussing the results for our GR models, we present here our simulations of three of the Newtonian models also studied by LCCS. We begin, however, with a description of the qualitative features of phase-transition-induced collapse of a rotating NS to an HQS which is relevant also for the later GR models.

4.1 Collapse dynamics and gravitational radiation waveform

The EOS of the deconfined quark matter in the stellar core generally gives a smaller pressure contribution than that of the hadronic

Table 2. Summary of the set of collapse models: γ is the adiabatic index of the hadronic matter during the evolution, δ is the EOS parameter that specifies the contribution of the quark matter pressure in the mixed phase, $\rho_{c,b}$ is the value of the central rest-mass density at bounce, $|h|_{max}$ is the maximum value of the GW signal strain during the evolution, E_{gw} is the energy emitted in GWs (during a total emission time of $t_f = 50$ ms), f_F and $f_{^2f}$ are the frequencies of the fundamental quasi-radial and quadrupolar modes, respectively, while τ_F and $\tau_{^2f}$ are the damping times of those modes in the GW signal. In addition, we give the phases ϕ_1 and ϕ_2 of the F and ^2f modes and the relative amplitude A_1/A_2 as obtained from a fit to the GW signal according to equation (B1). Note that the collapse models CA5, CB4 and CC3 are identical, as are models CB2 and CD2, and models CB5 and CD7. During the contraction, models CB6, CC4 and CD9 form an apparent horizon and become black holes. The phase-transition-induced collapse models CN1, CN2 and CN3, as well as the test collapse models CN $_{nipr}$ and CN $_{ipr}$ are computed with a Newtonian treatment. Where no values are given for the damping times, this signifies that the model either collapses to form a black hole or that no unambiguous damping could be diagnosed in the GW signal (mostly due to mode resonance; see Section 5.5).

Model	Initial model	γ	δ	$\rho_{c,b}$ (10^{14} g cm^{-3})	$\lvert h\rvert_{max}$ (10^{-23} at 10 Mpc)	E_{gw} (10^{-4} M$_\odot$ c^2)	f_F (kHz)	$f_{^2f}$ (kHz)	τ_F (ms)	$\tau_{^2f}$ (ms)	ϕ_1 (rad)	ϕ_2 (rad)	A_1/A_2
CA1	A1	2.00	2	15.81	1.45	0.04	0.87	2.01	40	12	0.06	−3.07	0.93
CA2	A2	2.00	2	16.04	1.33	0.29	0.99	2.08	49	130	−0.48	3.24	0.40
CA3	A3	2.00	2	15.81	1.90	0.59	1.05	2.08	–	18	−3.91	−6.44	0.15
CA4	A4	2.00	2	15.92	1.10	0.17	1.07	2.08	319	67	−0.15	0.30	0.64
CA5	A5	2.00	2	15.99	0.62	0.11	1.09	2.06	418	–	0.09	3.00	1.44
CA6	A6	2.00	2	16.02	0.52	0.11	1.12	2.04	270	51	−0.15	1.50	1.78
CA7	A7	2.00	2	16.10	0.25	0.05	1.16	2.02	711	–	−0.46	3.44	3.01
CA8	A8	2.00	2	16.07	0.09	0.01	1.19	2.00	–	–	5.98	6.35	1.69
CB1	B1	2.00	2	9.52	0.42	0.01	1.05	1.78	99	37	0.06	3.17	0.57
CB2	B2	2.00	2	11.70	0.69	0.05	1.06	1.90	133	44	0.04	3.06	0.71
CB3	B3	2.00	2	14.36	0.74	0.09	1.10	2.02	196	59	0.10	−3.11	0.87
CB4	B4	2.00	2	15.99	0.62	0.11	1.10	2.06	418	–	0.09	3.00	0.64
CB5	B5	2.00	2	17.92	2.41	1.16	1.08	2.10	687	76	6.16	6.02	0.06
CB6	B6	2.00	2	–	–	–	–	–	–	–	–	–	–
CC1	C1	2.00	2	10.31	0.36	0.01	1.14	1.76	143	53	0.13	3.21	0.77
CC2	C2	2.00	2	12.71	0.51	0.04	1.13	1.90	71	47	−0.03	3.27	0.86
CC3	C3	2.00	2	15.99	0.62	0.11	1.10	2.06	418	–	0.09	3.00	0.64
CC4	C4	2.00	2	–	–	–	–	–	–	–	–	–	–
CD1	B2	2.00	1	10.47	0.40	0.01	1.15	1.86	150	36	0.00	3.17	0.69
CD2	B2	2.00	2	11.70	0.69	0.05	1.07	1.90	133	44	0.04	3.06	0.71
CD3	B2	2.00	3	12.93	1.07	0.08	1.04	1.94	54	39	0.15	2.96	0.78
CD4	B2	2.00	4	14.16	1.47	0.14	1.10	1.96	19	48	0.35	−1.42	2.32
CD5	B2	2.00	5	15.35	1.84	0.15	1.14	1.97	8	44	0.04	3.17	0.80
CD6	B5	2.00	1	14.41	0.31	0.04	1.13	2.04	248	62	0.00	−3.18	1.04
CD7	B5	2.00	2	17.92	2.41	1.16	1.09	2.10	687	76	6.16	6.02	0.06
CD8	B5	2.00	3	24.80	1.14	0.24	1.02	2.15	–	34	−0.61	3.41	0.46
CD9	B5	2.00	4	–	–	–	–	–	–	–	–	–	–
CN1	N	1.95	1	10.37	4.41	0.88	2.68	1.98	73	80	3.17	0.00	1.12
CN2	N	1.85	1	12.31	15.38	4.10	2.88	2.14	9	20	2.95	−0.08	1.03
CN3	N	1.75	1	14.19	21.22	5.70	3.18	2.34	1	15	2.85	−0.38	0.98
CN$_{nipr}$	N	1.90	–	12.32	10.11	4.96	2.67	2.04	71	67	3.32	0.06	1.10
CN$_{ipr}$	N	2.00	–	11.82	7.63	2.86	2.83	2.04	86	67	2.97	−0.01	1.05

EOS[2] and so the phase transition in the NS core leads to an instability of the progenitor NS (which is in equilibrium before the transition) and the entire NS starts to contract. Depending on the parameters used and the phase transition time-scale, the infall phase typically lasts between 0.3 and 0.5 ms. As the pressure in the core rises with increasing density, the infall decelerates and the contraction of the inner core is stopped, while the outer regions are still falling in. In the case of a rotating NS, the deceleration of the core can be augmented by the increase of centrifugal forces due to angular momentum conservation in the contraction phase.

Because of its inertia, the core overshoots its new equilibrium configuration, rebounds, expands again and then recollapses. It typically experiences many such distinct sequences of infall, bounce and re-expansion in the form of pronounced, mainly radial ring-down pulsations until it finally reaches a new equilibrium state. Fig. 1 shows the time evolution of the central rest-mass density ρ_c for the Newtonian model CN2, where this oscillatory behaviour can be clearly seen.

If the initial NS is non-rotating, then the newly formed HQS pulsates only radially, and only $l = 0$ modes are present in the oscillation spectrum (unless significant convection develops). In this case, no GWs are emitted. However, if a rotating initial model undergoes a collapse and ring-down, then GWs of considerable amplitude can be emitted, as shown in the waveform plot in Fig. 2, again for model CN2.

Comparing a simple collapse model with a purely ideal gas EOS to a regular collapse model with a quark contribution to the EOS, LCCS demonstrated that the phase-transition-induced collapse of a rotating NS to an HQS predominantly excites two quasi-normal

[2] In principle, the quark matter could give as large a pressure contribution as the hadronic matter (see e.g. Alford et al. 2007a, for a recent discussion). However, in our study we do not consider those cases.

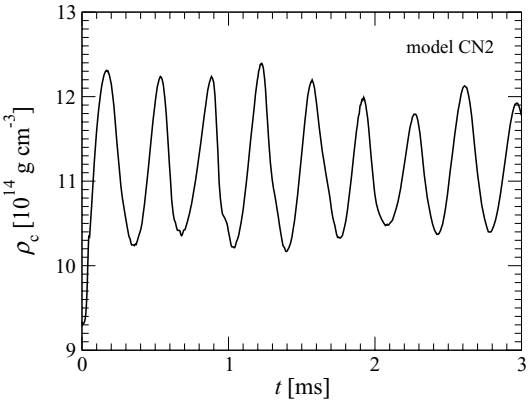

Figure 1. Time evolution of the central rest-mass density ρ_c for the Newtonian collapse model CN2 (which is identical to model R of LCCS).

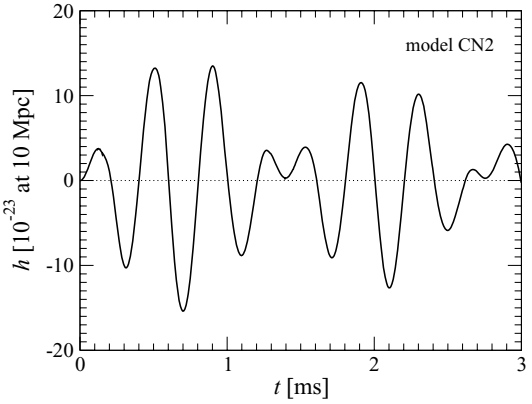

Figure 2. Time evolution of the GW strain h at a distance of 10 Mpc for the Newtonian collapse model CN2.

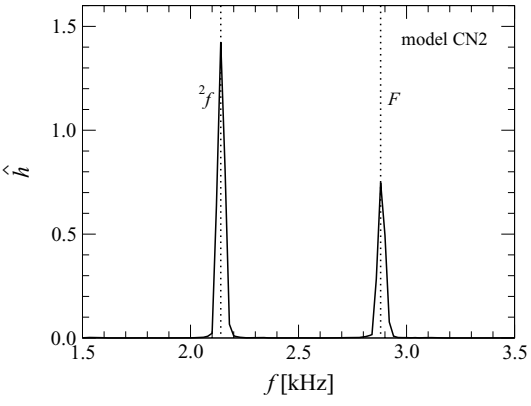

Figure 3. Power spectrum $\hat{h}$ (in arbitrary units) of the GW strain h for the Newtonian collapse model CN2. The narrow peaks of the F and ^2f modes clearly dominate the spectrum.

pulsation modes: the fundamental $l = 0$ quasi-radial F mode and the fundamental $l = 2$ quadrupolar ^2f mode. These stand out in the power spectrum of many fluid or metric quantities and, in particular, in that of the gravitational radiation waveform as presented in Fig. 3. All of our collapse models exhibit the predominance of these two modes as a generic feature.[3] For the more slowly rotating models, the contribution from higher order modes at higher frequencies can become comparable to that of the two fundamental $l = 0, 2$ modes, but these higher frequency modes have damping times that are significantly shorter than those of the fundamental modes and their impact on the waveform (and other quantities) dies out quickly.

Comparing our values of selected quantities describing the collapse dynamics with the corresponding ones in LCCS shows that our code is able to accurately reproduce the original results (see Table 3), despite being based on a different formulation of the hydrodynamic equations and utilizing a different coordinate system. Furthermore, Figs 1–3, which correspond to the data plotted in Figs 6, 7 (centre panel) and 12 (dashed line) of LCCS, also exemplify the excellent agreement both qualitatively and quantitatively. Making this comparison and demonstrating the good agreement obtained at a Newtonian level is important for removing possible doubts about the analysis which we present in the next subsection concerning the onset and development of convective instabilities.

4.2 The role of convection in generating differential rotation

A conspicuous difference from the results of LCCS that we observe in the simulations of Newtonian models performed with our code is the significantly *smaller* damping of the post-bounce oscillations. This is not only apparent from the much larger values that we find for the damping times τ_F and $\tau_{^2f}$ (see Table 3) but can also be noted by comparing our Figs 1 and 2 to the corresponding Figs 6 and 7 (centre panel) in LCCS. This has important consequences for the physical interpretation given in LCCS for the damping of the quasi-radial post-bounce pulsations: they suggested that the dominant damping mechanism is conversion of the kinetic energy of these pulsations into differential rotation. According to their discussion, another less significant part of that kinetic energy is lost when matter at the boundary of the HQS is ejected by shock waves, while yet another small amount of damping is due to numerical dissipation.

The 3D Newtonian code of LCCS used a coarser grid spacing than in our 2D GR calculations and this (together with some other possible numerical effects) would have led to a higher level of numerical dissipation. If the damping of post-bounce pulsations which they saw was indeed mostly caused by *physical* processes such as the transformation of kinetic energy into differential rotation or mass shedding at the boundary, then we would not have seen much smaller damping in our simulations for the same models. We therefore conclude that numerical dissipation actually did play a major role for the damping seen in the simulations of LCCS (although physical processes certainly also played a role).

Furthermore, if the observed exponential damping, which removes energy from the pulsations at a constant relative rate, were directly feeding the generation of differential rotation, there should be a simple correlation between the evolution time t and the increase in the quantity used as a measure of differential rotation by LCCS,

$$T_d = \frac{1}{2}\int \rho\, r^2 \sin^2\theta\, (\Omega - \bar{\Omega})^2\, \mathrm{d}V, \tag{17}$$

where $\Omega = r^{-1}\sin^{-1}\theta\, v_\phi$ is the local angular velocity with v_ϕ being the rotation velocity of the fluid, and $\bar{\Omega}$ is the volume averaged

[3] We perform the mode identification by perturbing equilibrium models that have similar structure to those of the collapse remnants using specific $l = 0$ and 2 trial eigenfunctions and analysing the response to these perturbations. This method is described in detail in LCCS.

Table 3. Comparison of various quantities as calculated in our simulations for the Newtonian collapse models CN1, CN2 and CN3 (top row for each model) with the results published by LCCS (bottom row). For each quantity we also give the relative difference between our results and theirs. Note that we multiply their values for $\langle \hat{h}^2 \rangle^{1/2}$ by $\sqrt{2}$ to undo the angular averaging and obtain $|h|_{\max}$. The values of $\rho_{\rm c,b}$ for models CN2 and CN3 are extracted from Figs 6 and 10 in their article, respectively, while for model CN1 they present no data from which to read off the central rest-mass density at the bounce.

Model	$\rho_{\rm c,b}$ (10^{14} g cm^{-3})		$\lvert h\rvert_{\max}$ (10^{-23} at 10 Mpc)		$f_{\rm F}$ (kHz)		f_{2f} (kHz)		$\tau_{\rm F}$ (ms)		τ_{2f} (ms)	
CN1	10.37	–	4.41	4 per cent	2.68	1 per cent	1.98	1 per cent	72.78	600 per cent	80.23	670 per cent
	–		4.24		2.66		2.00		10.39		10.42	
CN2	12.31	<1 per cent	15.38	<1 per cent	2.88	2 per cent	2.14	3 per cent	8.56	234 per cent	20.10	325 per cent
	12.30		15.41		2.82		2.08		2.56		4.73	
CN3	14.19	<1 per cent	21.22	2 per cent	3.18	2 per cent	2.34	4 per cent	1.45	245 per cent	14.51	474 per cent
	14.14		21.64		3.12		2.25		0.42		2.53	

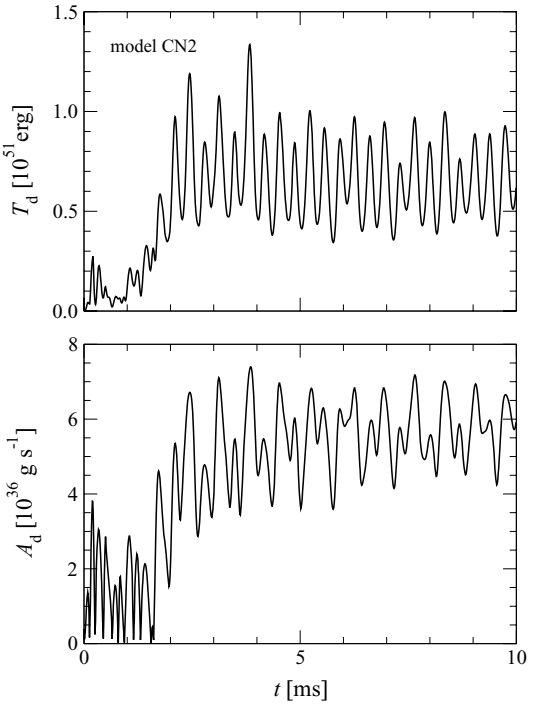

Figure 4. Time evolution of the differential rotation measures $T_{\rm d}$ (top panel) and $A_{\rm d}$ (bottom panel) for the Newtonian collapse model CN2.

angular velocity of the HQS.[4] Note that $T_{\rm d}$ does not follow the additive property for energies and so is not a fully satisfactory measure of the kinetic energy associated with differential rotation. We instead prefer to use as our measure of differential rotation, a quantity which is a volume-averaged and density-weighted measure of the relevant $r\phi$ component of the Newtonian shear tensor,

$$A_{\rm d} = \int \rho \left| \frac{{\rm d}v_\phi}{{\rm d}r} - \frac{v_\phi}{r} \right| {\rm d}V. \tag{18}$$

The two quantities (17) and (18) are related and they have similar time evolutions, as shown for model CN2 in Fig. 4 (and as found for all of the models considered), but we prefer to use $A_{\rm d}$ because of it having a clearer physical meaning.

Overall, the evolution of the two measures of differential rotation has the following general behaviour: after an initial peak associated with the initial collapse and the main bounce (with its height correlating with the intensity of the bounce), the average differential rotation stays roughly the same for around a millisecond (corresponding to several dynamical time-scales during which a number of post-bounce oscillations occur) following which it grows considerably up to a maximum value, then decreases a little and finally oscillates around an almost constant state. This behaviour is not in accordance with having continuous conversion of pulsational kinetic energy into differential rotation as the main damping mechanism. Rather, it suggests that some other process is responsible for creating the observed differential rotation.

The initial peak of $T_{\rm d}$ and $A_{\rm d}$ can be readily explained by the fact that any initially uniform rotation profile will become non-uniform during the collapse as a result of the non-homology of the collapse. On the other hand, the intermittent behaviour after the initial peak and the saturation at a constant value can be interpreted straightforwardly in terms of differential rotation caused by large-scale convection developing in the HQS several dynamical time-scales after the initial collapse when it is still pulsating but is already close to a new quasi-equilibrium state.

In rotating stellar models significant convection can occur if the Solberg–Høiland stability criteria are violated (see e.g. Cerdá-Durán, Font & Dimmelmeier 2007, and references therein). For our simple EOS, these translate into the condition that convection can develop if there is a sufficiently strong negative radial gradient of specific entropy (depending on the rotation rate of the HQS). We find that the method of pressure reduction employed by LCCS, which involves uniformly lowering γ in the ideal gas EOS (14) for the hadronic phase without adjusting the value for the internal specific energy ϵ at the initial time, indeed results in a very large negative specific-entropy gradient for their choices of γ. This is shown for model CN2 in Fig. 5 (solid line), where we plot the radial profile at $t = 0$ of the (density-dependent) measure of specific entropy

$$\tilde{K} = \frac{\rho\epsilon(\gamma - 1)}{\rho^\gamma} \tag{19}$$

in the equatorial plane, assuming an ideal gas EOS for the entire star with a γ that is reduced from its initial value of 2–1.85. Note that for a polytrope $\tilde{K}$ is identical to the polytropic constant K.

In order to assess unambiguously the occurrence of artificially produced convection and its impact on the development of differential rotation, we set up two simple Newtonian collapsing test

[4] Note that in contrast to LCCS, we averaged $\bar{\Omega}$ at each time level and not only once at the time of bounce, because when we did the latter, we obtained a very oscillatory behaviour for $T_{\rm d}$; we are not clear why LCCS did not observe this.

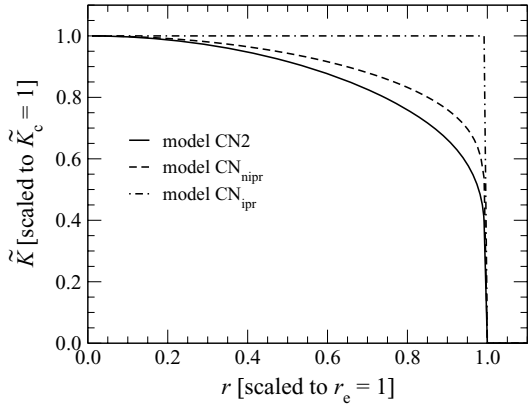

Figure 5. Radial profiles of the specific entropy measure $\tilde{K}$ (top panel) and of the r-component of its gradient (bottom panel), both calculated in the equatorial plane at the initial time for the Newtonian models CN2 (solid line), CN $_{\rm nipr}$ (dashed line) and CN$_{\rm ipr}$ (dash–dotted line). Both the entropy and the radius are scaled to give $\tilde{K}_{\rm c} = 1$ and $r_{\rm e} = 1$.

models, which are both based on the initial model N and utilize a purely ideal gas EOS (14), so as to simplify the discussion by removing the influence of quark matter on the results. In model CN$_{\rm nipr}$ (with non-isentropic pressure reduction) we reduce the pressure by lowering the adiabatic index γ from its initial value to 1.9 (without then adjusting ϵ); this creates a strong initial negative specific-entropy gradient that is comparable with the one in model CN2 (see Fig. 5). In model CN$_{\rm ipr}$ (for isentropic pressure reduction) γ remains at its pre-collapse value of 2 during the evolution, while the pressure reduction is now realized by a lowering the polytropic constant K by 10 per cent, which keeps the specific entropy uniform throughout the entire NS.

Note that the parameters in the EOS for these two test models have been chosen in such a way that the collapse dynamics (represented by the maximum density reached at the first bounce and the amplitude of the post-bounce pulsations) is comparable with that of model CN2, as can be seen from Fig. 6. Consequently, the gravitational radiation waveforms of these models also have amplitudes and waveforms similar to those of model CN2.

However, because of the different behaviour regarding convective instability, the dynamics of the three models CN2, CN$_{\rm nipr}$ and CN$_{\rm ipr}$ fall into two very distinct classes, depending on whether the initial pressure reduction creates a strong negative specific-entropy profile or leaves the specific entropy constant. In all models, analysis of the meridional velocity fields shows no noticeable convection being present at early times (e.g. at the time of the main bounce, around $t = 0.2$ ms). In the isentropic collapse model CN$_{\rm ipr}$ convection continues to remain unimportant also at later times and, accordingly, both $T_{\rm d}$ and $A_{\rm d}$ remain very small at all times (see the right-hand panel of Fig. 7). In stark contrast, the non-isentropic models CN2 and CN$_{\rm nipr}$ develop several convection vortices in the bulk of the collapsed star at $t \sim 1$ ms (corresponding to a few dynamical timescales), which is when the two differential rotation measures start to increase. This convection grows rapidly and reaches saturation almost instantaneously, with typical maximum convection velocities of $\sim$0.03 c. During the entire period when $T_{\rm d}$ and $A_{\rm d}$ are increasing, the convection remains practically constant and redistributes angular momentum and entropy locally within each vortex. By times $t \gtrsim 5$ ms this has led to the specific entropy being almost constant within the spatial scale of each convection vortex. Convection then subsides again, and $T_{\rm d}$ and $A_{\rm d}$ remain approximately constant from then on. It is clear, therefore, that the distinct phases in the time evolution of the two quantities reflect very accurately the distinct phases of convection, which acts as the mechanism that redistributes angular momentum and thus creates differential rotation.

The impact of angular momentum redistribution by convection on the initially uniform rotation profile can be seen from Fig. 8 which shows plots of the rotation velocity v_ϕ in the equatorial plane for the different models. For the strongly convective models CN2 (left-hand panel) and CN$_{\rm nipr}$ (centre panel), the v_ϕ curves are driven away from the initial uniform rotation (straight line) profile to reach a step-like profile at late times, whereas the essentially non-convective model CN$_{\rm ipr}$ (right-hand panel) maintains an approximately uniform rotation profile.[5]

It is worth stressing that the occurrence of convection here, and thus the creation of the differential rotation, is essentially independent of the presence and strength of post-bounce pulsations. Indeed, setting aside some small spurious convection close to the stellar boundary (caused by interaction of matter with the artificial low-density atmosphere), the strong *bulk* convection is caused by having a negative specific-entropy gradient and can be switched on and off at will, depending on whether the initial pressure reduction destroys isentropy or not.

In order to demonstrate this connection further, we constructed initial equilibrium models with a *local* polytropic EOS,

$$P = K(\rho)\, \rho^{\gamma}, \tag{20}$$

with $\gamma = 2$, where the polytropic 'constant' K (ρ) depends on the rest-mass density and thus varies inside the NS. By adjusting K (ρ) we can thus create models with negative (as well as positive) specific-entropy gradients of arbitrary strengths. When these initial models are evolved with an ideal gas EOS (14), they remain essentially in equilibrium, pulsating with only very small amplitudes. However, during the evolution they develop convection, and subsequently differential rotation, with a strength that directly corresponds to the strength of the negative specific-entropy gradient imposed initially. This is illustrated in Fig. 9 where we show plots of the meridional velocity field superimposed on the magnitude of the φ component of the vorticity. For this figure we selected three such equilibrium models for which the initial specific-entropy profile varies between constant specific entropy and a gradient that is comparable to model CN2.[6] Clearly, convection is practically nonexistent in the isentropic model (left-hand panel), whereas the model with moderate initial non-isentropy (centre panel) develops considerable convection in those parts of the NS that are not too far from the rotation axis. Finally, for the model with the strong negative initial specific-entropy gradient (right-hand panel), conspicuous convection vortices occur throughout the NS. Plots of the vorticity for collapsing models show similar patterns but there the meridional velocity field is also affected by the contribution from the large quasi-radial pulsations.

Also for these equilibrium models the time evolution of $A_{\rm d}$ exhibits the expected behaviour, as shown in Fig. 10 (we here no longer plot $T_{\rm d}$ which, however, exhibits a very similar time evolution to that of $A_{\rm d}$). Note that the quasi-periodic modulation of $A_{\rm d}$ is not caused by pulsations of the star, as their amplitudes are too small to be visible in $A_{\rm d}$ and they have higher frequencies. Instead,

[5] This rather good preservation of uniform rotation is a consequence of the infall being nearly homologous here.

[6] Note that these equilibrium models have central densities comparable with that of CN2 but they are more compact.

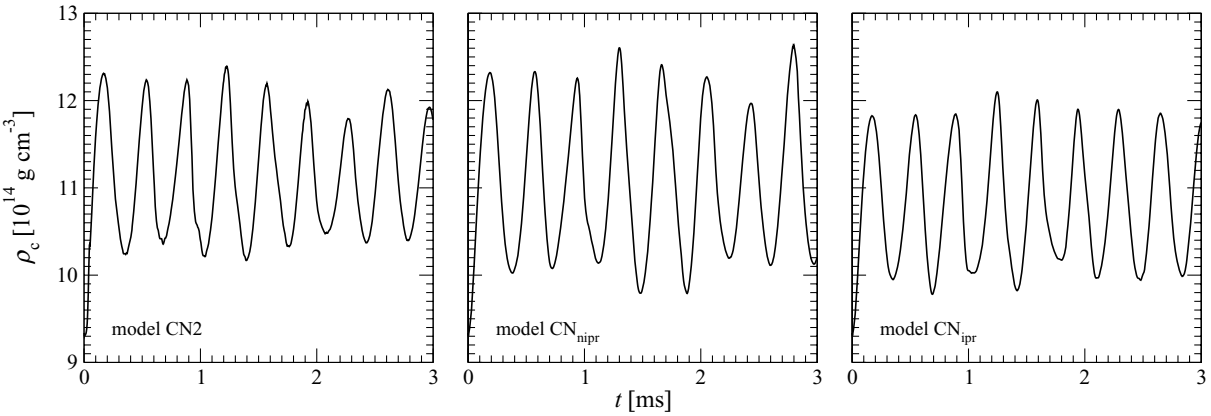

Figure 6. Time evolution of the central rest-mass density ρ_c for the Newtonian models CN2 (left-hand panel), CN_{nipr} (centre panel) and CN_{ipr} (right-hand panel).

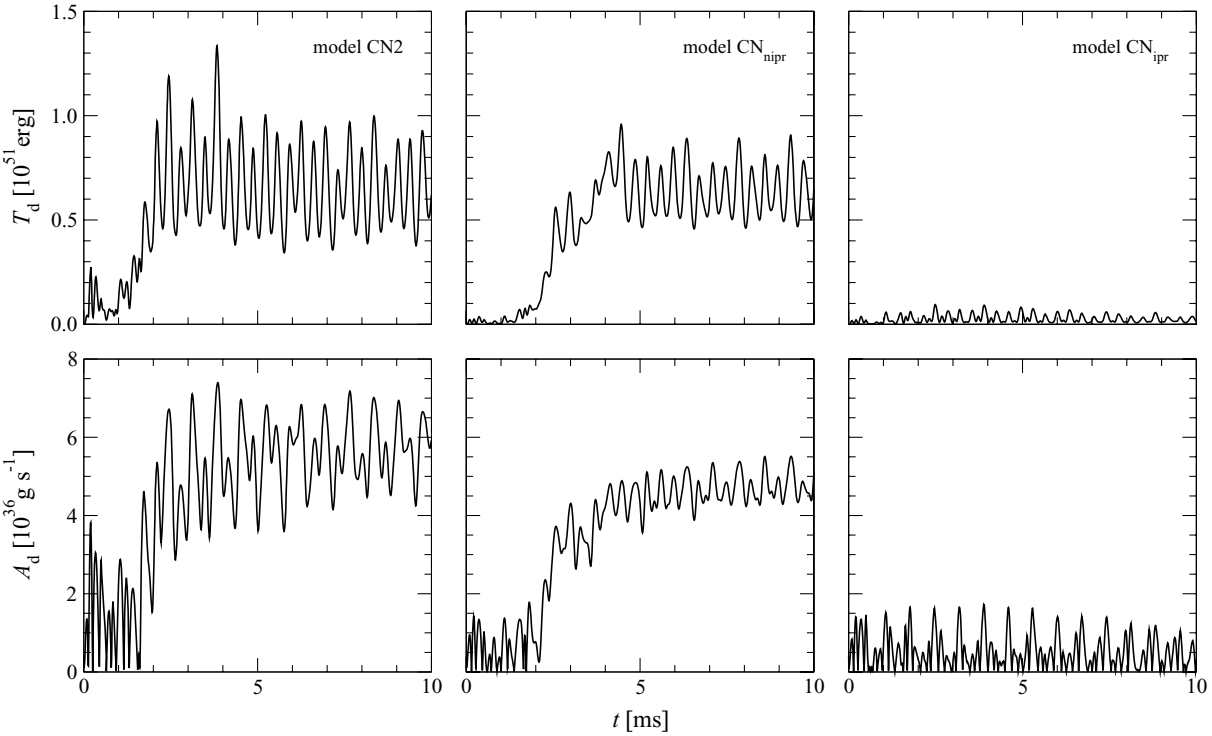

Figure 7. Time evolution of the differential rotation measures T_d (top row) and A_d (bottom row) for the Newtonian collapse models CN2 (left-hand panels), CN_{nipr} (centre panels) and CN_{ipr} (right-hand panels).

these oscillations (which can also be seen in a power spectrum of A_d for the collapse models CN2 and CN_{nipr}) are due to temporal variations in the vortices, with their time-scale being determined by the typical convection velocity and the average vortex size.

In summary, we find that the differential rotation reported by LCCS is almost exclusively caused by the transient convection that occurs if a negative specific-entropy gradient is generated by the initial pressure reduction. Therefore, we are convinced that the conclusion drawn by LCCS about the link between the damping of the large-amplitude post-bounce pulsations and the creation of differential rotation, although seemingly plausible, is not correct. They observed that the kinetic energy stored in the pulsations is approximately equal to the maximum value of A_d for both model CN2 and model CN3 (their models R and G1.75; see their fig. 8) but this is an unfortunate coincidence. Our models CN_{nipr} and CN_{ipr} demonstrate that convection and thus the maximum value of A_d can vary enormously for roughly constant pulsation amplitude.

5 GENERAL RELATIVISTIC COLLAPSE MODELS

5.1 Collapse dynamics and gravitational radiation waveform

We next present our results for the GR models, employing a quark contribution to the EOS that is slightly different from that used for the Newtonian models (see Section 3.2). Overall, we have performed simulations for 23 different models, and in Table 2 we

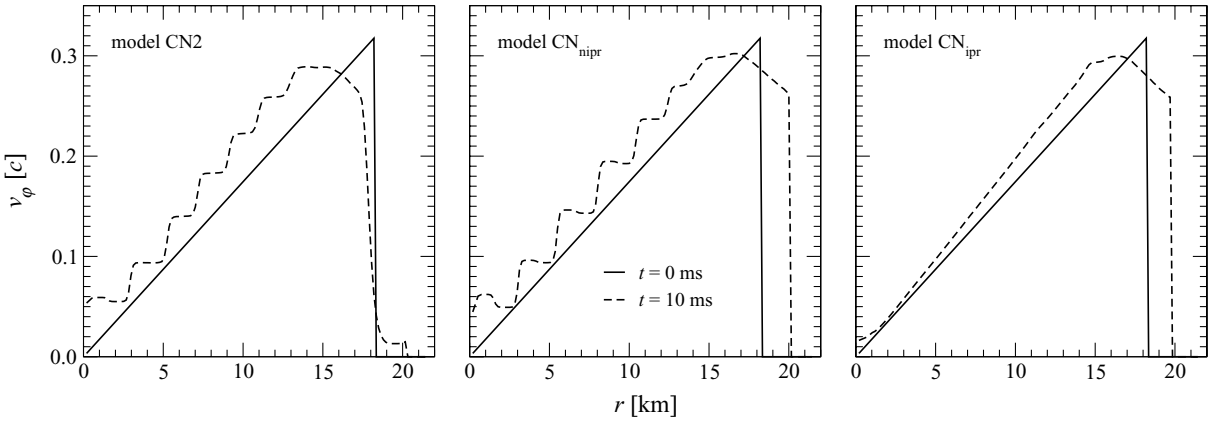

Figure 8. Radial profile of the rotation velocity v_ϕ in the equatorial plane for the Newtonian collapse models CN2 (left-hand panel), CN_{nipr} (centre panel) and CN_{ipr} (right-hand panel) at the initial time (solid lines) and at $t = 10$ ms (dashed lines). For models that develop considerable convection, the initially uniform rotation profile is locally destroyed.

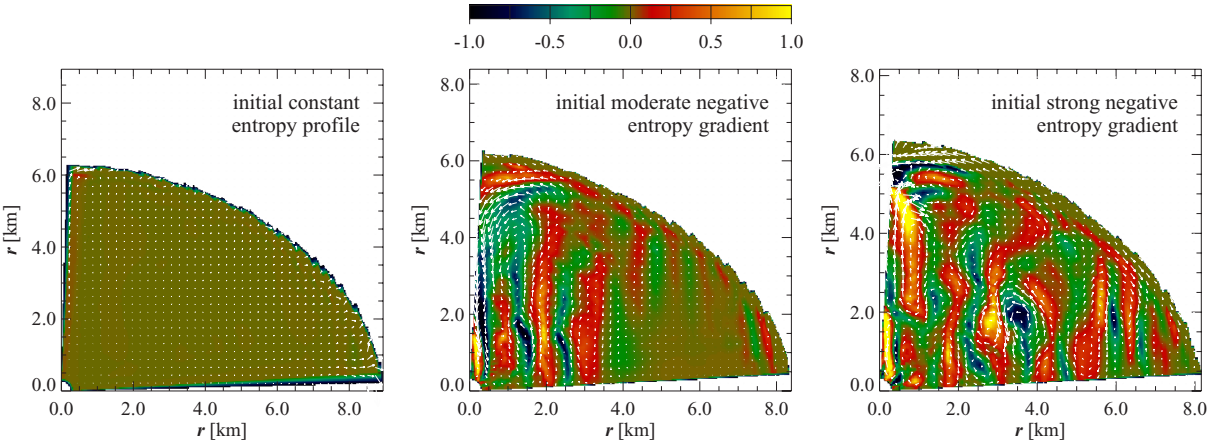

Figure 9. The velocity field $v_{r,\theta}$ in the meridional plane (with the rotation axis being in the vertical direction) and the colour-coded magnitude of the φ component of the vorticity are shown for equilibrium models whose initial specific-entropy profile is, respectively, constant (left-hand panel), comparable to model CN2 (right-hand panel) and roughly halfway between those two cases (centre panel). The evolution time is at $t = 3.5$ ms when convection (if present) has saturated. The length-scale of the vectors is the same for all three models, with the maximum length corresponding to $\sim 0.03c$. The vorticity is measured in arbitrary units.

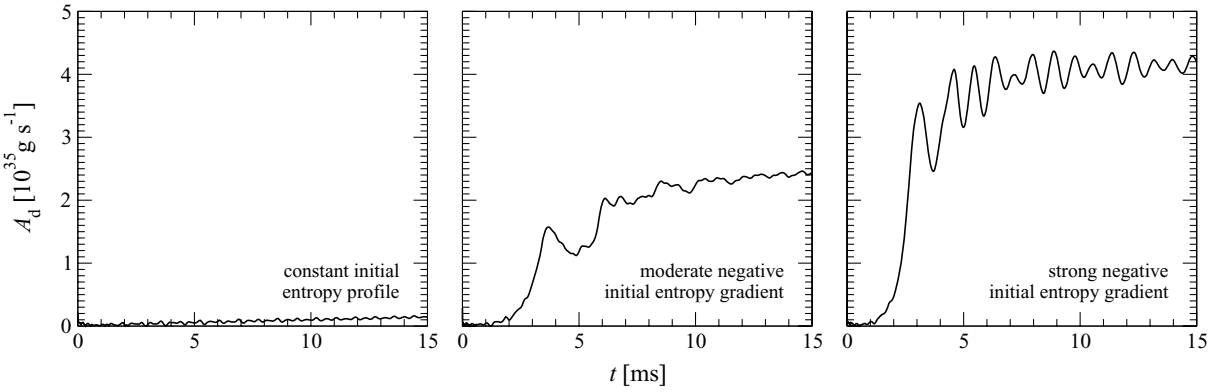

Figure 10. Time evolution of the differential rotation measure A_d for equilibrium models whose initial specific-entropy profile is, respectively, constant (left-hand panel), comparable to model CN2 (right-hand panel) and roughly halfway between these two cases (centre panel). For the isentropic model, A_d remains very close to zero at all times and is barely visible in the plot.

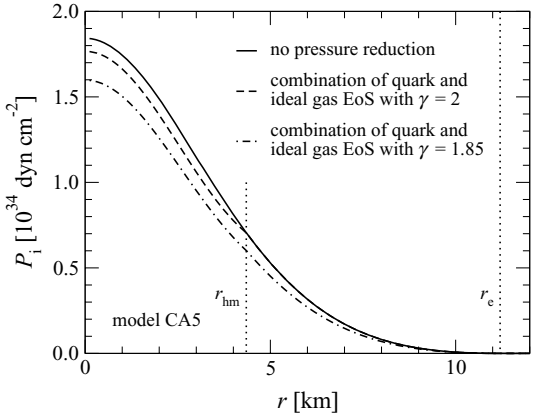

Figure 11. Radial profile of the initial pressure P_i in the equatorial plane for the GR collapse model CA5 without any pressure reduction (solid line), with the regular EOS treatment (combination of quark and ideal gas EOS with $\gamma = 2$; dashed line) and with the EOS description used by LCCS (combination of quark and ideal gas EOS with $\gamma = 1.85$; dash–dotted line). In the latter case P is reduced throughout the star and not just where $\rho > \rho_{hm}$. The vertical dotted lines mark the radius $r_{hm} = 4.35$ km where $\rho = \rho_{hm}$ and the equatorial radius $r_e = 11.2$ km of the initial NS.

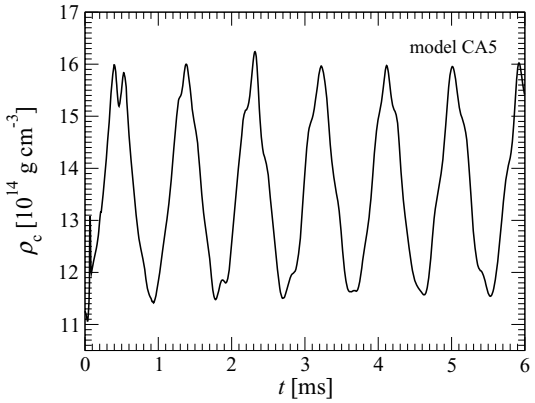

Figure 12. Time evolution of the central rest-mass density ρ_c for the GR collapse model CA5.

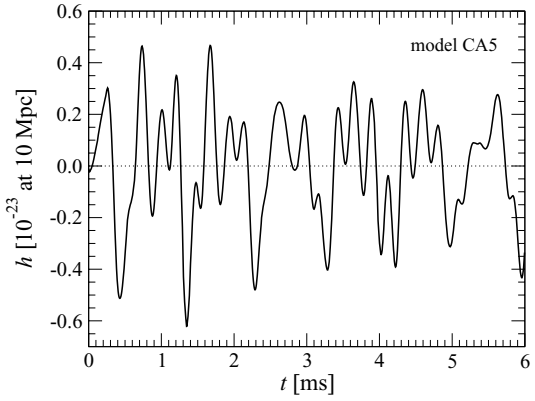

Figure 13. Time evolution of the GW strain h at a distance of 10 Mpc for the GR collapse model CA5.

summarize the most important quantities which characterize the dynamics of each model.

As discussed previously, our prescription for the triggering of the phase transition and of the subsequent collapse differs from the one proposed by LCCS in that we do not change the adiabatic index γ, leaving the EOS in the hadronic phase unchanged. Although still very idealized, we believe that this represents a more consistent description of the physics of the phase transition. As a consequence of this prescription, the phase transition and collapse in our GR models is solely caused by the lower pressure exerted by matter which is transformed to the quark phase. The difference between our approach and that of LCCS is exemplified in Fig. 11, where we show the different prescriptions for the initial pressure reduction when applied to the representative model CA5.

With our prescription, only a small (central) part of the NS loses pressure support, and thus the NS will not, in general, collapse to a black hole even if the initial model is close to the stability limit. Rather, it reaches a new stable equilibrium state in the form of an HQS. For instance, in model CA5 only $0.49\,M_\odot$ out of a total mass of $1.75\,M_\odot$ is subject to the pressure reduction. Nevertheless, the change of the central rest-mass density during the contraction from its initial value $\rho_{c,i}$ to $\rho_{c,b}$ at bounce reaches values of up to $\sim$50 per cent for some models (see Tables 1 and 2), which is comparable to what was obtained by LCCS in their Newtonian models with a larger overall pressure reduction. There are at least two different reasons behind this large and *local* increase of ρ: first, the stronger gravitational force that the NS experiences in a GR framework naturally amplifies the strength of the collapse. Secondly, our initial equilibrium models (in particular the ones with high $\rho_{c,i}$) are already close to the limit beyond which the F mode becomes unstable. For these models, therefore, even a moderate perturbation can lead to a strong local contraction and trigger post-bounce oscillations of significant amplitude.[7]

[7] For a non-rotating HQS with the EOS of equation (15) the unstable branch starts at $\rho_c = 29.6 \times 10^{14}$ g cm^{-3}.

Despite this conceptually important difference in the way that the phase transition (and hence the resulting collapse) is triggered, no major *qualitative* differences appear when comparing results from the GR simulations with those from the Newtonian simulations of LCCS. This is shown for the representative model CA5 in Figs 12 and 13, where we plot the time evolution of the central rest-mass density ρ_c and the GW strain h, respectively. We point out, however, that in our GR models of sequences CA, CB, CC and CD we observe a small spike in the time evolution of the central rest-mass density ρ_c at about 0.1 ms (see Fig. 12). This spike is caused by a density compression wave triggered by the non-uniform pressure reduction in those models, which at the start of the evolution leads to a noticeable gradient in the first radial derivative of the pressure at the interface between the mixed and pure hadronic matter phases.

As in the Newtonian case, the waveform is mainly composed of the fundamental $l = 0$ quasi-radial F mode and of the fundamental $l = 2$ quadrupolar ^2f mode (see the Fourier spectrum of the GW signal in Fig. 14). However, in contrast to the Newtonian models, the F mode is now at a lower frequency than the ^2f mode (with the F mode now having frequencies between 0.87 and 1.19 kHz for our selection of models, and the ^2f mode having frequencies between 1.76 and 2.15 kHz). This difference is a consequence of the different density profile in the GR case and is in agreement with previous investigations of pulsating $\gamma = 2$ equilibrium polytropes (see Dimmelmeier, Stergioulas & Font 2006a, and references therein).

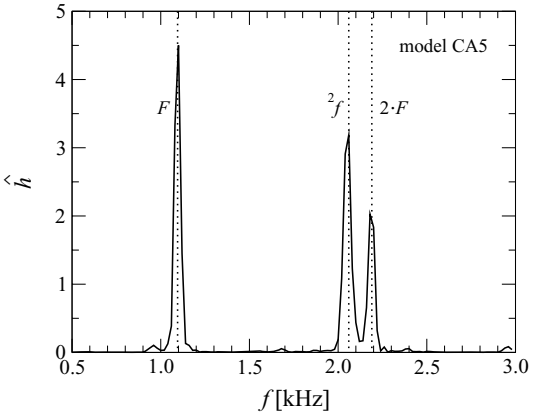

Figure 14. Power spectrum $\hat{h}$ (in arbitrary units) of the GW strain h for the GR collapse model CA5. The narrow peaks of the F and ^2f modes (along with a prominent non-linear self-coupling of the F mode) clearly dominate the spectrum.

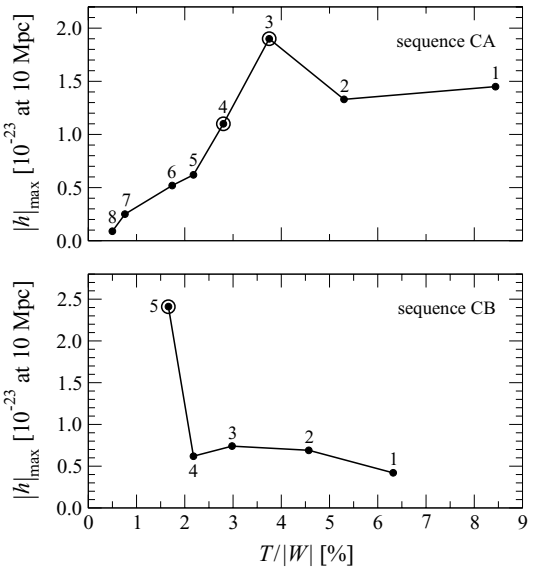

Figure 15. Dependence of $|h|_{max}$ on the initial rotation strength $T/|W|$ for the collapse model sequences CA (top panel) and CB (bottom panel). Each model is denoted with a filled circle, and models with enhanced GW emission due to mode resonance (see Section 5.5) are shown with an additional large circle.

The prominent peak next to that for the ^2f mode is a non-linear self-coupling of the F mode at twice the original frequency, which (like several other such non-linear modes) is strongly excited due to the violent nature of the collapse. Using the fitting procedure described in Appendix B, we have extracted from the waveforms the damping times for these two modes, obtaining values between $\tau_F = 8$ and 687 ms, and $\tau_{2f} = 18$ and 130 ms, respectively. Because of the much smaller numerical dissipation of our code, the damping times computed for the GR models are considerably longer than those for the Newtonian models calculated by LCCS.

Another important quantitative difference with respect to the Newtonian models appears in the maximum GW strain $|h|_{max}$ that is significantly smaller here for comparable overall rotation rates. The deeper gravitational potential well in GR gives a shorter contraction time-scale and higher densities at bounce, which tend to amplify the GW signal, while this is counteracted by the more compact collapsed remnant in GR having a smaller quadrupole moment (for a detailed discussion of these two competing effects, see Dimmelmeier et al. 2002b). However, the main reason for $|h|_{max}$ here being smaller than for the Newtonian models is that within our scenario for the destabilization, a smaller proportion of the total matter content of the NS is directly involved in the collapse and in undergoing large density variations. For a source at 10 Mpc, $|h|_{max}$ ranges between 0.08 and 1.72×10^{-23} for all of the models considered here, while the energy E_{gw} emitted in GWs during the first 50 ms of the evolution ranges between 10^{-6} and $10^{-4}\,M_\odot c^2$. A more detailed discussion about the detectability of these sources is presented in Section 5.6.

5.2 Influence of rotation, total rest mass and composition of the mixed phase

We next investigate the impact on the collapse dynamics of varying the values of the main model parameters: the initial rotation period p, the rest mass M_0, and the exponent δ used in the mixed phase.

Rotation. As in any gravitational collapse, the influence of rotation is twofold. On the one hand, the rotational flattening of the collapsing fluid produces an increase of the quadrupole moment, which could potentially lead to stronger GW emission. On the other hand, centrifugal forces also tend to slow down the collapse and, in cases where they are strong enough, they can considerably reduce the time variation of the quadrupole moment and hence the GW amplitude.

For the sequence CA, in which the initial central rest-mass density $\rho_{c,b}$ is kept constant, the dependence of the maximum GW strain $|h|_{max}$ on the rotation rate is rather straightforward to interpret (see the top panel of Fig. 15 and Table 2). Except for models CA3 and CA4, whose expected GW emission is altered by resonance effects (as discussed in detail in Section 5.5), $|h|_{max}$ increases monotonically with increasing rotation (which we here measure in terms of the ratio $T/|W|$, as this quantity turns out to remain almost constant throughout the evolution). Since in this sequence the values of the central rest-mass density at bounce are all close to 16×10^{14} g cm^{-3}, we conclude that centrifugal forces do not significantly retard the collapse for these models and so there is no significant associated weakening effect for the GW emission.

The effect of rotation is also investigated in the constant rest-mass sequence CB, for which we observe a slight initial increase of $|h|_{max}$ with increasing rotation (see the bottom panel of Fig. 15) that is then reversed for very rapid rotation (model CB5, whose GW emission is again enhanced by mode resonance, is an exceptional case). We attribute this behaviour to the fact that in this sequence the central rest-mass density, both in the initial model and at bounce, drops significantly as rotation grows along the sequence, resulting in a much less violent collapse. This property can be seen in the central overdensity at bounce, which amounts to $\rho_{c,b}/\rho_{c,i} - 1 = 39$ per cent for model CB5, but reaches only 13 per cent for model CB1. The interplay of growing rotation and decreasing collapse strength then explains the behaviour of the GW peak amplitude seen for sequence CB.

The influence of rotation on the frequencies of the F and ^2f modes can be compared directly with the results of Dimmelmeier et al. (2006a), who obtained relations between the frequencies of these two modes and the strength of rotation for pulsating equilibrium models of NSs with a $\gamma = 2$ polytropic EOS, both for sequences with constant central rest-mass density and with constant rest mass. In agreement with that work, for our dynamical collapse models,

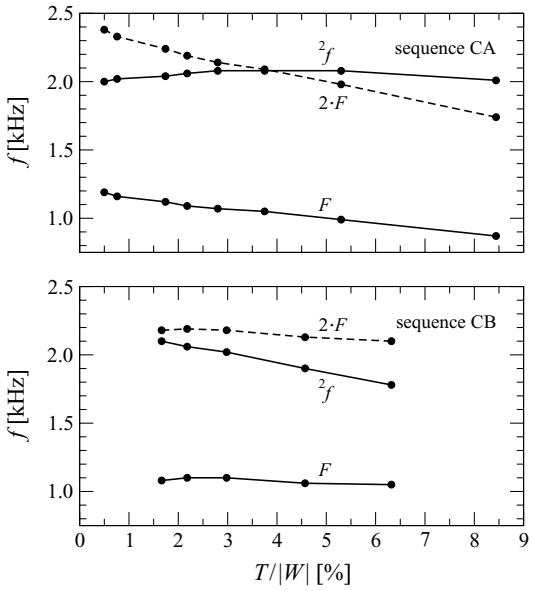

Figure 16. Dependence of the mode frequencies $f_{\rm F}$, $f_{^2f}$ and $f_{2\cdot F}$ on the initial rotation strength $T/|W|$ for the collapse model sequences CA (top panel) and CB (bottom panel). Each model is marked by a filled circle.

$f_{\rm F}$ decreases noticeably with more rapid rotation for sequence CA and CB, as shown in Fig. 16 (see also Table 2). Also, for $f_{^2f}$ our models reproduce the initial increase and subsequent decrease with growing rotation for the constant initial central rest-mass density sequence CA (sequence BU in Dimmelmeier et al. 2006a) as well as the monotonic decrease with increasing rotation for the constant rest-mass sequence CB (their sequence AU). Our results therefore demonstrate that studies of linear pulsations of equilibrium models can be used also in the more general context of stellar gravitational collapse to predict the dependence of the fundamental mode frequencies on rotation. In our models, the creation of differential rotation by non-homologous contraction during the collapse phase is rather small. However, even if the deviation from uniform rotation were stronger, the study of Dimmelmeier et al. (2006a) suggests that the influence on the mode frequencies would still be weak.

In Fig. 16 we also show the behaviour of the non-linear self-coupling of the F mode at twice the original frequency (the 2·F mode) which is strongly excited in all of our models (see also Fig. 14) including the Newtonian ones. Such non-linear couplings of linear quasi-normal modes were also observed in the study of initially linearly perturbed equilibrium models by Dimmelmeier et al. (2006a), although at much lower excitation levels. In contrast to the initial low-level perturbations used in their models, in our case the strong collapse and rebound at bounce manages to channel a large amount of energy into this particular mode. A detailed discussion of the impact of exciting the 2·F mode for GW emission is presented in Section 5.5.

Rest mass. For their Newtonian models, LCCS reported that along a sequence with constant rotation period p, the maximum GW strain $|h|_{\rm max}$ first increases with M_0 and then decreases again. In contrast, we find that for our corresponding sequence CC, $|h|_{\rm max}$ increases monotonically with M_0 (see Table 2).[8] This different behaviour is probably due to a fundamental difference between our GR models and their Newtonian counterparts. Besides the obvious differences in the structure of the HQS and hence in the mode frequencies, one should bear in mind that the rest mass of the GR models has an upper limit corresponding to the point of transition to the unstable branch of equilibrium solutions. This is particularly evident for sequence CC, where model CC4 does not reach a stable configuration after the collapse but instead produces a black hole as deduced from the appearance of an apparent horizon. As a result, the eventual decrease of $|h|_{\rm max}$ with increasing M_0 in the Newtonian case may not occur in GR simply because it might require rest masses above the upper limit.

Composition of the mixed phase. The impact on the collapse dynamics of varying the parameter δ (and hence varying the pressure reduction due to the presence of the quarks in the mixed phase) is quite obvious. Both for the collapse models CD1–CD5, which are based on the initial model B2, and for the models CD6–CD9, which use the initial model B5, the rest-mass density at bounce $\rho_{\rm c,b}$ and the amplitude of the post-bounce oscillations grow when the pressure reduction is enlarged by increasing the exponent δ (see Table 2). Since within each of the two subsequences the initial rotation rate is constant, the growth of $\rho_{\rm c,b}$, and hence of the compactness, with a greater pressure reduction is directly reflected in stronger GW emission and higher values for $|h|_{\rm max}$. Also in this case, an exception arises with model CD7 which is identical to the already mentioned model CB5. Interestingly, when $\delta = 4$, the pressure reduction in the mixed phase is so great that the corresponding model CD9 collapses directly to a black hole without experiencing a bounce.

Finally, we note that the F-mode frequencies in the sequence of models CD1–CD5 first decrease with increasing δ and then increase again. This may be the result of a near cancellation of opposite effects: while a larger pressure reduction produces a higher overall density of the post-collapse HQS (potentially resulting in higher values of $f_{\rm F}$), it also leads to more rapid rotation due the comparatively greater compactness (which should lower $f_{\rm F}$). We also note that the large-amplitude quasi-radial oscillations in the last model(s) of each subsequence of sequence CD are so strongly damped shortly after the collapse, that making a precise determination of the frequency $f_{\rm F}$ is difficult.

5.3 Damping of the stellar pulsations

Both from the values for the damping time $\tau_{\rm F}$ of the fundamental quasi-radial F mode in the GW signal given in Table 2 and from Fig. 17, where we plot the time evolution of $\rho_{\rm c}$ for the most and least rapidly rotating collapse models of sequence CA, it is evident that there can be significant damping of the post-bounce pulsations in the HQS, for some values of the model parameters. In Table 4 we also report the values for the damping time $\tau_{{\rm F},\rho_{\rm c}}$ extracted from the time evolution of the central rest-mass density $\rho_{\rm c}$: these values range from 8 to 200 ms for the models considered here. With the exception of those models for which the GW emission is dominated by mode resonance, the two estimated time-scales $\tau_{\rm F}$ and $\tau_{{\rm F},\rho_{\rm c}}$ are very similar.

In Section 4, we have argued that the kinetic energy stored in the quasi-radial post-bounce pulsations is not responsible for generating differential rotation, and therefore the observed damping cannot be attributed to this mechanism as previously suggested. Since, also, the numerical dissipation of our code is much too small to be the main cause for the strong damping observed in some models (and anyway affects all models in the same way) it is necessary to offer an alternative physical explanation for why the pulsations are strongly

[8] We have found the same qualitative behaviour also for another sequence with constant period $p = 1.4$ ms and varying rest mass, for which we do not present the data here.

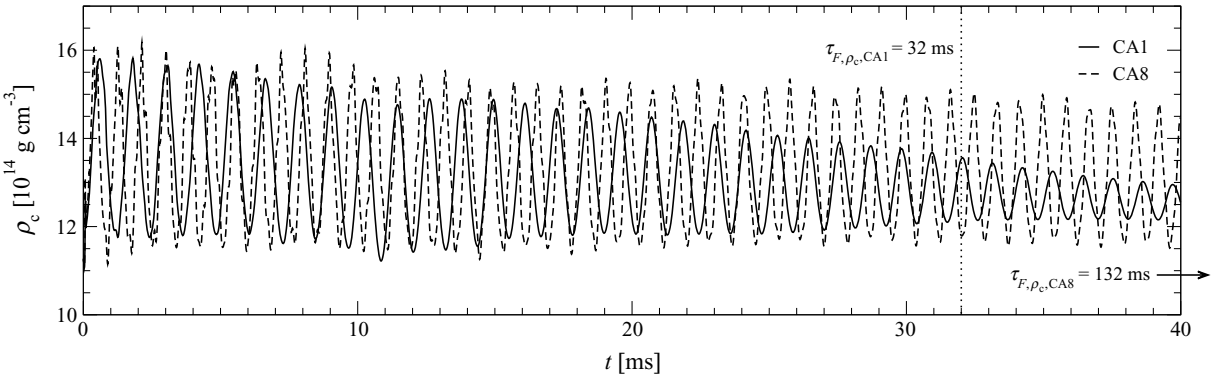

Figure 17. Time evolution of the central rest-mass density ρ_c for models CA1 and CA8, the most and the least rapidly rotating models of sequence CA. The dotted line marks the pulsation damping time τ_{F,ρ_c} for model CA1.

Table 4. Relevant quantities for mass-shedding-induced damping: p is the rotation period of the NS, p_K is the rotation period of a free particle on a circular orbit at the equator (Kepler limit), p/p_K is the ratio of these two periods, $\rho_{c,b}/\rho_{c,i} - 1$ is the central overdensity at bounce compared to the initial value, and τ_{F,ρ_c} and τ_F are the F mode damping times extracted from the time evolution of ρ_c and from the GW signal, respectively. Note that we omit here those models that collapse to a black hole. For completeness, we also include the Newtonian collapse models CN1, CN2 and CN3.

Model	p (ms)	p_K (ms)	p/p_K	$\rho_{c,b}/\rho_{c,i} - 1$ (per cent)	τ_{F,ρ_c} (ms)	τ_F (ms)
CA1	1.00	0.89	1.12	41	32	40
CA2	1.20	0.75	1.60	43	36	49
CA3	1.40	0.72	1.94	41	93	–
CA4	1.60	0.70	2.29	42	155	319
CA5	1.80	0.69	2.61	42	160	418
CA6	2.00	0.68	2.94	42	150	270
CA7	2.99	0.67	4.46	43	152	711
CA8	5.98	0.66	9.06	43	132	–
CB1	1.30	0.89	1.46	13	113	99
CB2	1.40	0.80	1.75	23	128	133
CB3	1.60	0.73	2.19	35	156	196
CB4	1.80	0.69	2.61	42	160	418
CB5	2.00	0.67	2.99	52	103	687
CC1	1.80	0.79	2.28	18	136	143
CC2	1.80	0.74	2.43	29	62	71
CC3	1.80	0.69	2.61	42	160	418
CD1	1.40	0.80	1.75	10	200	150
CD2	1.40	0.80	1.75	23	128	133
CD3	1.40	0.80	1.75	36	49	54
CD4	1.40	0.80	1.75	49	19	19
CD5	1.40	0.80	1.75	62	8	8
CD6	1.40	0.80	1.75	22	191	248
CD7	2.00	0.67	2.99	52	103	687
CD8	2.00	0.67	2.99	110	53	–
CN1	1.20	0.86	1.40	11	91	73
CN2	1.20	0.86	1.40	32	16	9
CN3	1.20	0.86	1.40	52	1	1

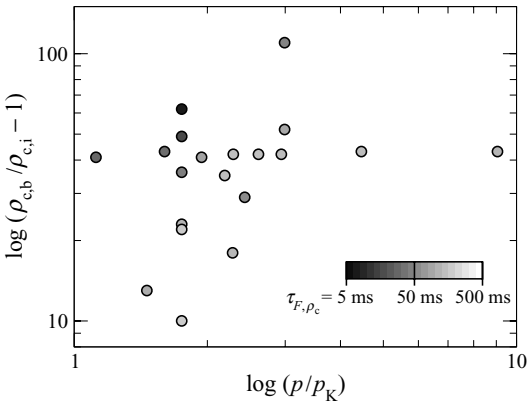

Figure 18. Location of all GR collapse models in the (p/p_K) – $(\rho_{c,b}/\rho_{c,i} - 1)$ plane. The damping time τ_{F,ρ_c} of the F mode, as calculated from the time evolution of the central rest-mass density, is encoded in the grey-scale, with dark/light grey corresponding to strong/weak damping. Only models with very rapid rotation (close to the Kepler limit) *and* violent post-bounce oscillations due to a very dynamical collapse (upper left-hand corner of the plot) have short damping times.

damped for some models, with τ_{F,ρ_c} being a few ms (and thus comparable with the dynamical time-scale), while for other models the damping is much slower, with $\tau_{F,\rho_c} \sim 100$ ms (and thus orders of magnitude longer than both the dynamical time-scale and the pulsation period of the star; in this case, the damping seems to be limited essentially to that caused by numerical viscosity). Since the gravitational radiation back reaction on the system is also negligible (and is not taken into account by our conformally flat approximation of the metric equations anyway), the strong damping seen can only be due to hydrodynamic effects.

A careful analysis of our model parameters reveals that damping is significant only for those models that both rotate very rapidly *and* experience strong pulsations. This can be seen in Fig. 18, where the value of τ_{F,ρ_c} for each model is given by the grey-scale. Only models located in the upper left-hand part of the plane spanned by the rotation period ratio p/p_K and the overdensity at bounce $\rho_{c,b}/\rho_{c,i} - 1$ have the very short damping times.

For models rotating close to the mass-shedding limit (the Kepler limit), the effective gravity near to the equator is significantly weakened, vanishing at the mass-shedding point. As one goes to models having larger amplitude quasi-radial post-bounce pulsations, an increasing amount of matter is ejected from low latitudes on the stellar surface during each oscillation. This matter goes into the initially artificial very-low-density atmosphere and creates an expanding envelope of weakly bound (or even unbound) material around the HQS. This mass shedding causes strong damping of the pulsations, as pulsational kinetic energy is converted into gravitational potential energy of the ejected matter. Since polar perturbations (mainly

radial ones) are coupled to axial perturbations in rotating stars, the damping rapidly affects all modes.

This mass-shedding-induced damping of oscillations in rapidly rotating NSs near to the Kepler limit was first observed and discussed by Stergioulas, Apostolatos & Font (2004) for weakly pulsating equilibrium polytropic NS models in uniform rotation, treated within the Cowling approximation (neglecting the dynamics of the space–time). In a subsequent study, Dimmelmeier et al. (2006a) found that if the Cowling approximation is abandoned and the space–time is dynamically evolved, the effect of mass-shedding is drastically reduced, giving a consequent decrease in the damping of the pulsations. However, both of these studies treated small-amplitude pulsations of equilibrium models (working within the linear regime), whereas in our collapse models the pulsations can have very large amplitudes.

Considering the example of model CD8: this has a large initial pulsation amplitude, with relative variations in ρ_c of around 55 per cent (which is about half of the overdensity at bounce) but it is rotating too slowly to be close to the Kepler limit (with $p/p_K \simeq 3$) and does not show strong damping. The five models with the shortest damping time-scales, however, ($\tau_{F,\rho_c} < t_f = 50\,\mathrm{ms}$) all have both quite large initial pulsation amplitudes >18 per cent and are also rapidly rotating, with rotation period ratios $p/p_K < 1.75$. This is consistent with equatorial mass-shedding being the predominant mechanism for the strong damping of the post-bounce pulsations seen for models that both rotate close to the Kepler limit *and* pulsate with large amplitude. For models that are not affected by equatorial mass shedding, other damping mechanisms predominate (such as the conversion of kinetic energy into internal energy by shocks, nonlinear coupling of modes, numerical or physical dissipation) but all of these operate on time-scales much longer than the dynamical time-scale.[9]

5.4 The role of convection

As discussed above, the damping of post-bounce pulsations and the development of differential rotation seen by LCCS seems to have been mainly a manifestation of the convective motion artificially produced in their simulations by the way in which they induced the collapse. Real physical convection might well be induced by energy input coming from the phase transition but this has no connection with the artificially induced convection. Calculating the real convection is beyond the scope of the present simplified treatments and remains a topic for future work. While we have eliminated from our calculations the main source of artificial convection present in the LCCS simulations, some artificially induced convection still remains. There are at least two different origins for this which apply for two different classes of initial models.

The first origin is related to the CFC approximation itself: when the data from the initial model solver are mapped to the evolution code and the initial-value problem is subsequently resolved to satisfy the constraints (3), small errors due to the CFC approximation create spurious departures from constant entropy. This side effect of the CFC approximation is clearly larger for rapidly rotating and very compact models such as CA1, and becomes very small for slowly rotating models, vanishing in the non-rotating limit. Fig. 19 shows the initial radial profile of the specific-entropy measure $\tilde{K}$ (cf. equation 19) for model CA1, together with those for the Newtonian models CN1 and CN3 discussed previously. It can be seen that the CFC approximation produces a negative specific-entropy gradient for model CA1 at the start of the evolution. While this gradient is very small in the bulk of the star (for $r/r_e \lesssim 0.8$), near to the surface it becomes comparable to (or even greater than) that for model CN1, for which γ was initially decreased from 2 to 1.95. However, it is still much smaller than that occurring when reducing γ to 1.75 as in model CN3.

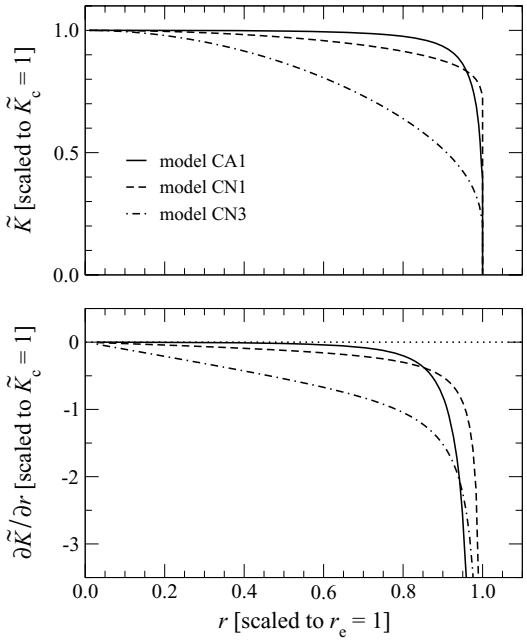

Figure 19. Radial profile of the specific-entropy measure $\tilde{K}$ (top panel) and its radial derivative (bottom panel) in the equatorial plane at the initial time for the GR model CA1 (solid line), and the corresponding profiles for the Newtonian models CN1 (dashed line) and CN3 (dash–dotted line). The specific-entropy measure and the radius are scaled to give $\tilde{K}_c = 1$ and $r_e = 1$.

The CFC-induced violation of the Solberg–Høiland criteria drives this model (and other rapidly rotating ones) to develop significant convection, which we measure in terms of the general relativistic equivalent of the averaged shear (cf. equation 18),

$$A_d = \int \sqrt{\gamma}\,\rho h W^2 \left| \frac{dv_\phi}{dr} - \frac{v_\phi}{r} \right| dV, \qquad (21)$$

where $v_\phi = \sqrt{v_3 v^3}$ is the rotation velocity of the fluid.[10] Fig. 20 shows the time evolution of A_d for model CA1 (whose convection is, in fact, among the strongest for the GR models; left-hand panel), as well as for the Newtonian models CN1 (centre panel) and CN3 (whose convection is among the strongest for the Newtonian models; right-hand panel). It can be seen that both the development of the convection with time for model CA1 and its maximum saturation level are comparable with those for the Newtonian model CN3, while the convection in model CN1 is stronger and occurs on a much

[9] As far as viscosity is concerned, in the quark phase the shear viscous damping time-scale is comparable to that of normal nuclear matter, which is of the order of 10^8 s for a typical NS, while the bulk viscous damping time-scale is of the order of seconds, assuming a rotation period $p = 1$ ms and an s quark mass $m_s = 100$ MeV (Madsen 2000).

[10] As already noted for the Newtonian models, the Newtonian equivalent of A_d has a qualitatively very similar behaviour to that of T_d but only the first of these has a clearly defined physical meaning.

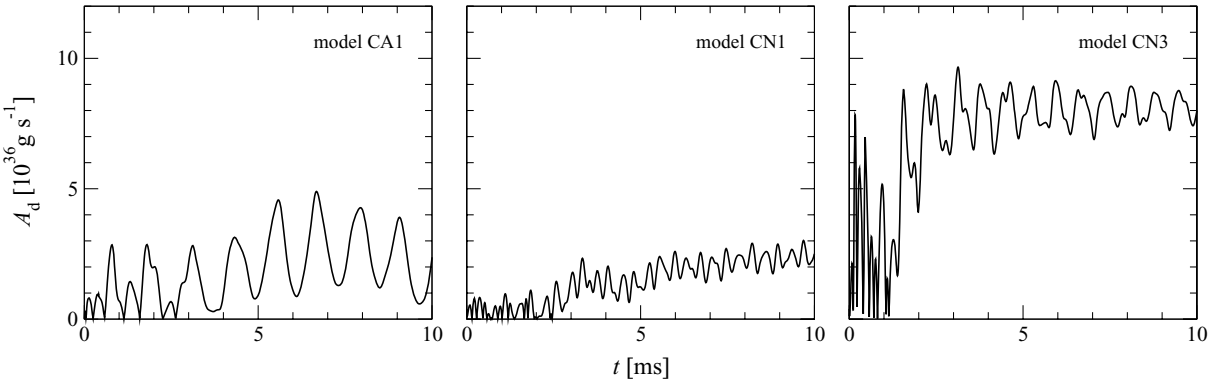

Figure 20. Time evolution of the differential rotation measure A_d for the GR collapse model CA1 (left-hand panel) and the Newtonian collapse models CN1 (centre panel) and CN3 (right-hand panel).

shorter time-scale, which is natural since the initial non-isentropy is larger in that case.

The second origin of spurious convection appears in slowly rotating models; this is not due to the CFC approximation since the errors coming from that are essentially negligible in these cases. Instead, convection is produced here by the small violation of isentropy caused by interaction of the matter just inside the surface of the HQS with the surrounding artificial atmosphere. This perturbation slowly propagates inwards and finally affects the entire star at late times. Since in uniformly rotating configurations, centrifugal forces tend to have a stabilizing effect within the Solberg–Høiland criteria, it is easy to understand why this process occurs only for the slowly rotating models. An example of this mechanism in action is given by model CA8, which is the slowest rotator in our set of GR models: here A_d reaches a maximum that is close to the saturation level of models CA1 and CN1 but is still much smaller than the value for the strongly convective model CN3.

In models that are neither very rapidly nor very slowly rotating (e.g. model CC1), convection is almost absent and A_d remains at very low values, which can be explained as resulting from small deviations away from homology during the initial contraction and the subsequent post-bounce oscillations. We repeat, however, that consistent treatment of other possible real sources of convection remains a major topic for future work.

5.5 Enhanced emission of gravitational waves via mode resonance

In Section 5.2 we have discussed the influence of the initial rotation speed on the frequencies of the post-bounce oscillations and also commented that for models with the same rest mass, those with higher rotation generally have higher GW strain due to their increased quadrupole moments. This is indeed what is seen, for instance, in the sequence CB as reported in Table 2. This general behaviour, however, has a notable exception in the case of the comparatively slowly rotating model CB5, which has by far the largest GW strain for any of those in the sequence CB, with the energy emitted in GWs in the first 50 ms being at least an order of magnitude larger than for any of the other models in this sequence.

In the top panels of Fig. 21 we plot the time evolution of the central rest-mass density ρ_c for models CB3, CB4 and CB5. It can be seen that the collapse dynamics of model CB5 are not qualitatively different from those of the more rapidly rotating members of the same sequence. As rotation decreases from CB3 to CB5, the strength of the contraction increases, leading to higher central over densities $\rho_{c,b}$ at the bounce and stronger post-bounce oscillations. This, however, cannot account satisfactorily for the very large maximum GW strain amplitude $|h|_{max}$ of model CB5, nor for the growth of h during the first 20 ms *after* the bounce in this case (see bottom panels of Fig. 21).

Rather, the time evolution of h in model CB5 (the delayed growth, the saturation and the subsequent decay) suggests the presence of a resonance effect among several modes, at least one of which should be an efficient emitter of GWs. One of the obstacles to having strong GW emission is that the modes which are most strongly excited during the bounce are (quasi-)radial modes which are not efficient GW emitters; indeed they would not emit at all if rotation were not present to introduce non-radial contributions. However, it was suggested many years ago (see e.g. Eardley 1983) that the pulsational energy from a quasi-radial mode, which contains a significant amount of kinetic energy but radiates GWs only weakly, could be transferred to a much more strongly radiating quadrupolar mode by means of resonance effects and even parametric instabilities. Dimmelmeier et al. (2006a), as well as Passamonti et al. (2005) and Passamonti, Stergioulas & Nagar (2007) have discussed this possibility in the context of non-linear coupling of quasi-normal modes for nearly equilibrium models of NSs.

In order to investigate whether this mechanism might be responsible for the enhanced GW emission observed for model CB5, we performed a mode analysis for models CB3, CB4 and CB5. The power spectrum of the time evolution of the central rest-mass density ρ_c, shown in the top panels of Fig. 22, indicates that there is a lot of energy in the 2·F mode which has a peak about an order of magnitude higher than the corresponding one for the ^2f mode, located at slightly lower frequencies. As rotation decreases from model CB3 to model CB5, the frequencies of these two modes get closer until the two peaks almost merge for model CB5, with the relative difference between the two frequencies decreasing to about 4 per cent (see the bottom panel of Fig. 16 and also Table 5).[11] Under these conditions of resonance, the 2·F mode is able to transfer a considerable amount of energy into the ^2f mode, as can be clearly seen in the power spectrum of the waveform amplitude shown in the lower panels of Fig. 22. If the spectra for model CB5 from Fig. 16

[11] We have also performed simulations for models with other parameter values in the close vicinity of those for model CB5 and found that CB5 actually exhibits almost the maximum possible resonance between the 2·F and ^2f modes.

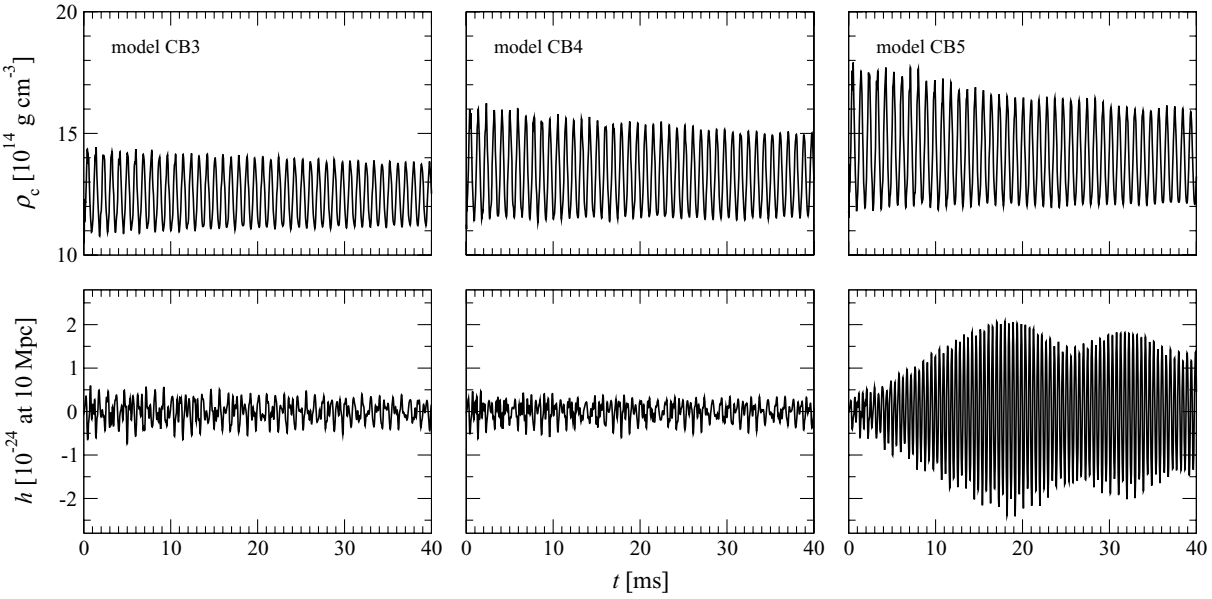

Figure 21. Time evolution of the central rest-mass density ρ_c (top panels) and the GW strain h at a distance of 10 Mpc (bottom panels) for the GR collapse models CB3 (left-hand panels), CB4 (centre panels) and CB5 (right-hand panels). The enhanced GW emission for model CN5 due to mode resonance is clearly visible.

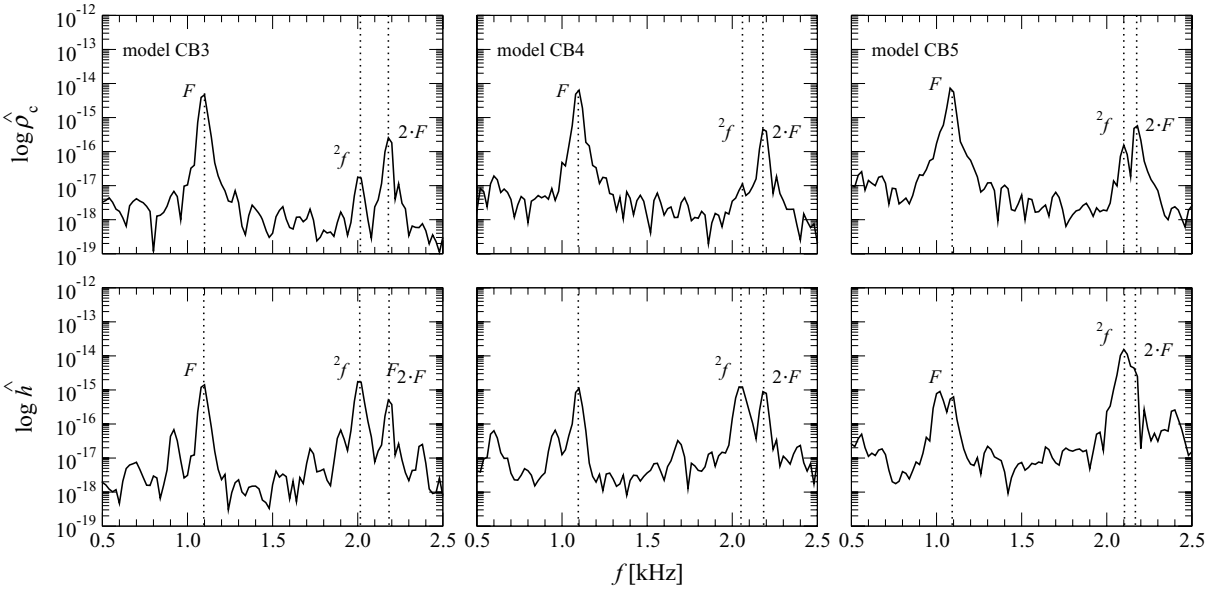

Figure 22. Logarithmic power spectrum (in arbitrary units) of the central rest-mass density ρ_c (top panels) and the GW strain h (bottom panels) for the same models as in Fig. 21. The resonance between ^2f and 2·F modes sets in as their frequencies (marked by dotted lines) approach each other.

are produced for several time windows, this energy transfer between the two modes becomes visible. While the peaks of both ρ_c and h corresponding to the ^2f mode first gradually grow in the early phases of the evolution (showing the initial amplification at the expense of the 2·F mode) and start decreasing only at later times, the peaks of the 2·F mode always decrease.

The strong dependence of the maximum GW strain $|h|_{max}$ on the rotation rate, as seen in Table 5 as well as in the bottom panel of Fig. 15, indicates that the resonant behaviour becomes important only when the frequencies of the ^2f and 2·F modes are very close to each other. This small difference between the two frequencies is also responsible for the clear beating pattern seen in the waveform for model CB5 (see the bottom right-hand panel in Fig. 21). Fig. 15 also shows that while the pulsation energy contained in the F mode (represented by the spectrum of ρ_c in the top panel) is always larger than the corresponding one in the 2·F mode, when more resonance between the 2·F and ^2f modes is at work, the 2·F mode becomes a very efficient emitter of GWs as well (see the spectrum of h in the lower panel), surpassing the F mode here. This is most likely a consequence of the altering of the 2·F mode's previously quasi-radial eigenfunction by the interaction with the quadrupolar ^2f mode (see e.g. Dimmelmeier et al. 2006a).

Applying this analysis to the complete set of investigated models, we find that the same resonance between the ^2f and 2·F modes is also

Table 5. The frequencies $f_{^2f}$ and $f_{2\cdot F}$ of the fundamental quadrupolar ^2f mode and the self-coupling of the F mode, for the collapse models of sequence CB. $\Delta f_{\rm rel} = f_{2\cdot F}/f_{^2f} - 1$ is the relative difference between the frequencies of these two modes.

Model	$f_{^2f}$ (kHz)	$f_{2\cdot F}$ (kHz)	$\Delta f_{\rm rel}$ (per cent)	$\lvert h\rvert_{\rm max}$ ($c10^{-23}$ at 10 Mpc)	$E_{\rm gw}$ ($10^{-4}\,{\rm M}_\odot\,c^2$)
CB1	1.78	2.10	18	0.38	0.01
CB2	1.90	2.13	12	0.57	0.05
CB3	2.02	2.18	8	0.10	0.09
CB4	2.06	2.19	6	0.10	0.11
CB5	2.10	2.18	4	1.72	1.16

at work in models CA3 and CA4 (this is clearly visible in the top panel of Fig. 15) as well as in model CD8. Also in these cases, the waveforms show an initial growth in amplitude over several cycles and then a strong beating at later times. In the case of model CD8, the growth in h due to the mode resonance becomes prominent long after the bounce, at $t \gtrsim 20$ ms, not reaching its maximum $|h|_{\rm max}$ until $t \simeq 48$ ms, when the quasi-radial oscillations have already been damped to around 38 per cent of their initial amplitude. In contrast, for models whose GW emission is not influenced by this resonance, $|h|_{\rm max}$ is reached at the time of bounce or very close to it. In addition, here the spectral power of both the 2·F and ^2f modes decreases at all times if successive spectra are obtained with the technique of shifted time windows.

5.6 Detectability prospects for the gravitational wave emission

Although the maximum GW strain $|h|_{\rm max}$ in the waveforms of our GR models is about an order of magnitude smaller than that computed by LCCS for Newtonian models, the long quasi-periodic GW emission that is possible for phase-transition-induced collapse may still make this scenario a plausible source for GW detectors. Assuming that the strong post-bounce oscillations are not damped by any other physical mechanisms apart from dissipation of kinetic energy by shocks, the damping times that we obtain suggest that the effective total emission time for GWs can be much longer than the time for which we have followed the evolution of our models ($t_{\rm f} = 50$ ms), extending to hundreds of oscillations.

The main GW emission modes are the F and ^2f modes, which have comparable energies in the power spectra, except where the resonance between the ^2f and 2·F modes is important, when the combined ^2f mode/2·F mode dominates the GW spectrum. Model CA5, for which we show in Fig. 23 the power spectrum of the time evolution of $\rho_{\rm c}$ (top panel) and of the GW signal (bottom panel), is an example where the frequencies of ^2f mode and 2·F mode are already close and the two modes start to merge.

Exploiting the fact that, for most models, the waveform can be very well approximated as a combination of two essentially monochromatic damped sinusoids, it is straightforward to construct a phenomenological waveform expressed in terms of six parameters: the mode frequencies $f_{\rm F}$ and $f_{^2f}$, the damping times $\tau_{\rm F}$ and $\tau_{^2f}$, and the initial phases and relative amplitude of the two modes (all of which can be found from Table 2). This can then be applied as a template in matched filtering data analysis algorithms so as to search for the waveforms in the data stream more effectively.

In order to assess the prospects for detection by current and planned interferometric detectors, we next calculate characteristic quantities for the GW signal following Thorne (1987). Making a Fourier transform of the dimensionless GW strain h,

$$\hat{h} = \int_{-\infty}^{\infty} {\rm e}^{2\pi {\rm i} f t} h \, {\rm d}t, \tag{22}$$

we can compute the (detector-dependent) integrated characteristic frequency

$$f_{\rm c} = \left(\int_0^{\infty} \frac{\langle \hat{h}^2 \rangle}{S_h} f \, {\rm d}f \right) \left(\int_0^{\infty} \frac{\langle \hat{h}^2 \rangle}{S_h} \, {\rm d}f \right)^{-1} \tag{23}$$

and the dimensionless integrated characteristic strain

$$h_{\rm c} = \left(3 \int_0^{\infty} \frac{S_{h\,{\rm c}}}{S_h} \langle \hat{h}^2 \rangle f \, {\rm d}f \right)^{1/2}, \tag{24}$$

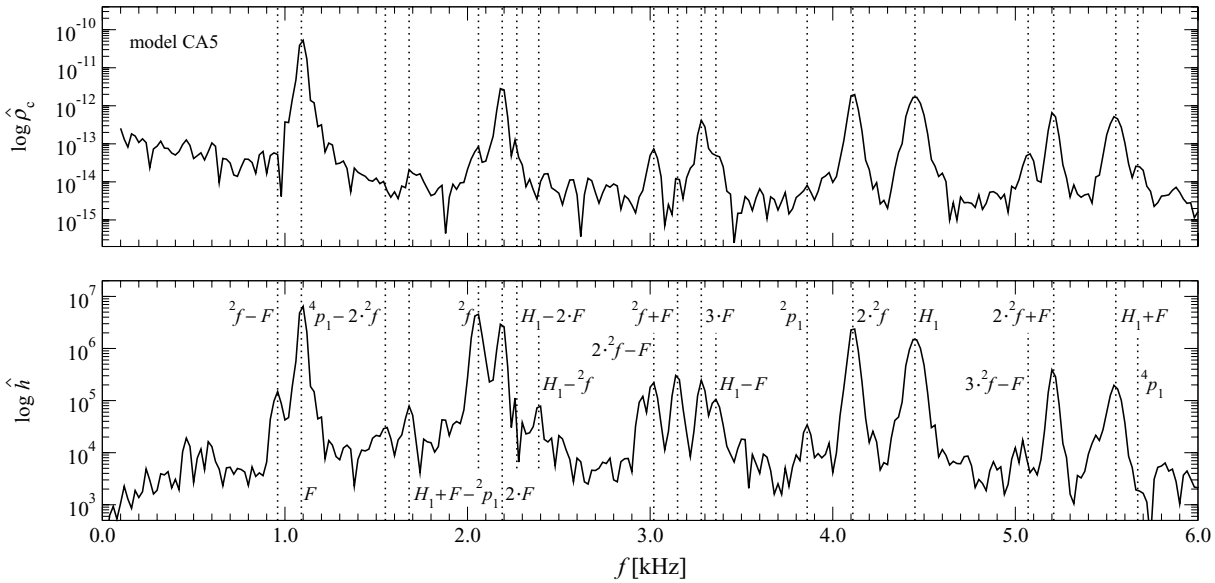

Figure 23. Logarithmic power spectrum (in arbitrary units) of the central rest-mass density $\rho_{\rm c}$ (top panel) and the GW strain h (bottom panel) for the GR collapse model CA5. The linear quasi-normal modes and the non-linear (self-)couplings are marked with dotted lines and labelled. H_1 denotes the first overtone of the F mode, while $^2p_1$ and $^4p_1$ are the first overtones of the fundamental $l = 2$ and 4 modes, respectively.

Table 6. Detection prospects for the GWs: f_c is the characteristic frequency, h_c is the integrated characteristic GW signal strain and S/N is the signal-to-noise ratio, each given for the current LIGO and VIRGO detectors, and for the future advanced LIGO detector. The values given for all of the quantities assume a total emission time of $t_f = 50$ ms and are dependent on the rms strain noise h_{rms} of the detector. Note that models CB6, CC4 and CD9 collapse to form a black hole as a result of the phase transition and so are omitted here.

Model	$f_{c,LIGO}$ (kHz)	$f_{c,VIRGO}$ (kHz)	$f_{c,adv.\,LIGO}$ (kHz)	$h_{c,LIGO}$ $(10^{-20}$at 10 kpc$)$	$h_{c,VIRGO}$ $(10^{-20}$at 10 kpc$)$	$h_{c,adv.\,LIGO}$ $(10^{-20}$at 10 kpc$)$	S/N LIGO (at 10 kpc)	S/N VIRGO (at 10 kpc)	S/N adv. LIGO (at 10 kpc)
CA1	0.954	0.978	1.029	2.55	2.59	2.68	7.5	12.0	179
CA2	1.755	1.798	1.864	5.65	5.75	5.92	6.8	11.8	201
CA3	1.845	1.876	1.923	8.52	8.63	8.80	9.4	16.6	287
CA4	1.619	1.660	1.735	3.56	3.62	3.75	4.8	8.3	139
CA5	1.349	1.382	1.450	1.78	1.81	1.87	3.1	5.3	86
CA6	1.415	1.452	1.527	1.55	1.58	1.63	2.5	4.4	71
CA7	1.449	1.485	1.572	0.72	0.73	0.76	1.1	2.0	32
CA8	1.609	1.672	1.788	0.29	0.30	0.31	0.4	0.7	11
CB1	1.349	1.374	1.417	1.31	1.33	1.36	2.3	4.0	64
CB2	1.304	1.335	1.388	2.12	2.16	2.22	3.9	6.7	108
CB3	1.322	1.353	1.411	2.09	2.12	2.18	3.8	6.4	104
CB4	1.349	1.382	1.450	1.78	1.81	1.87	3.1	5.3	86
CB5	2.073	2.078	2.086	13.18	13.27	13.24	12.3	21.9	389
CC1	1.370	1.394	1.435	1.06	1.08	1.10	1.8	3.1	51
CC2	1.370	1.394	1.442	1.48	1.50	1.54	2.6	4.4	71
CC3	1.349	1.382	1.450	1.78	1.81	1.87	3.1	5.3	86
CD1	1.346	1.370	1.407	1.23	1.25	1.27	2.2	3.7	61
CD2	1.304	1.335	1.388	2.12	2.16	2.22	3.9	6.7	108
CD3	1.313	1.345	1.406	2.79	2.84	2.93	5.1	8.7	140
CD4	1.555	1.585	1.636	4.54	4.60	4.71	6.5	11.2	188
CD5	1.661	1.682	1.718	5.09	5.14	5.23	6.6	11.6	197
CD6	1.350	1.383	1.449	0.82	8.36	0.86	1.5	2.5	40
CD7	2.073	2.078	2.086	13.18	13.21	13.24	12.3	22.0	389
CD8	1.722	1.780	1.862	3.88	3.99	4.13	4.8	8.3	141

where S_h is the power spectral density of the detector and $S_{h\,c} = S_h(f_c)$. We approximate the average $\langle\hat{h}^2\rangle$ over randomly distributed angles by $\hat{h}^2$, assuming optimal orientation of the detector. From equations (23) and (24) the signal-to-noise ratio (S/N) can be calculated as $h_c/[h_{rms}(f_c)]$, where $h_{rms} = \sqrt{f S_h}$ is the value of the rms strain noise for the detector (which gives the theoretical sensitivity window).

In Table 6 we summarize the values of f_c, h_c and the S/N for all of the models (except those which collapse to a black hole) for the currently operating LIGO and VIRGO detectors and for the future advanced LIGO detector. For all of the detectors we consider a source inside our own Galaxy at a reference distance of 10 kpc. The proportion of NSs that undergo phase-transition-induced collapse at some stage in their lifetimes is not well known. The phenomenon could occur at, or soon after, the formation stage (giving an event rate roughly proportional to that for core collapse supernovae) or it could come at a later stage when an old NS is spun up and has its mass increased by accretion from a binary partner in an LMXB (an interesting case but with an event rate which is thought to be very much lower, probably $\sim 10^{-5}\,\mathrm{yr}^{-1}$ for the Milky Way; see Pfahl, Rappaport & Podsiadlowski 2003). Another point is that a phase-transition-induced collapse occurring for an NS which is not rapidly rotating would not be so interesting for our purposes. Even under the most extremely optimistic assumption that the phase-transition-induced collapse rate equals that for core-collapse supernovae, that would only give a rate of up to 1 per 20 yr for our Galaxy, which is prohibitively low. On the other hand, if such an event did occur in our Galaxy, for current interferometric detectors of the LIGO class and assuming an emission time $t_f = 50$ ms, all of our models except one have an S/N above 1. For the strongest emitting model CB5, where mode resonance significantly enhances the GW emission, the S/N even exceeds 10. With the advanced LIGO detector, the S/N lies comfortably above 10 for all models and reaches almost 400 in model CB5.

For substantially increasing the event rate, it would be necessary for the detector to be sensitive to signals coming from distances out to the Virgo cluster, at $\sim$20 Mpc (for which the supernova rate would rise to more than 1 per year). However, at this distance the S/N for our models drops to well below 1 even for advanced LIGO. Therefore, as for GW signals from supernova core collapse (see the discussion in Dimmelmeier et al. 2005), the second generation detectors will improve the S/N of a local event, but will not increase the event rate much on account of the inhomogeneous galaxy distribution in the local region of the Universe. Only third generation detectors will have the required sensitivity in the kHz range to achieve a robust S/N at the distance of the Virgo cluster.

Note that for most of the models the *integrated* characteristic frequency f_c given in Table 6 is not very close to either of the two main GW emission frequencies f_F and $f_{^2f}$. This is because f_c reflects the frequency dependence of the sensitivity of the detector, because non-linear mode couplings and higher order linear modes also contribute to the GW signal (although with lower relative amplitudes; see Fig. 23) and, most importantly, because for many models the GW power spectrum of the signal exhibits nearly equally strong peaks in the F and ^2f modes.

The detector dependence of f_c and h_c is also illustrated in Fig. 24, where the locations of the GW signals for all of the models are plotted relative to the rms strain noise h_{rms} of the current LIGO

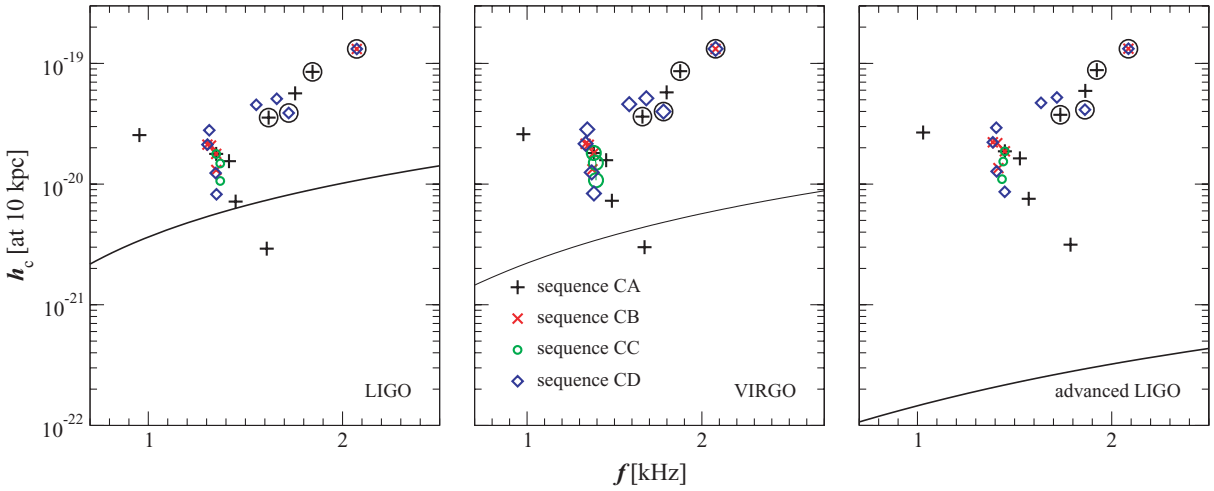

Figure 24. Location of the GW signals from all of our GR models in the h_c–f_c plane shown relative to the sensitivity curves (giving the rms strain noise h_{rms}) for the current LIGO detector (left-hand panel) and VIRGO detector (centre panel) and for the advanced LIGO detector (right-hand panel). The sources are taken to be at a distance of 10 kpc. Note that some of the models belong to more than one sequence. Models for which mode resonance boosts the GW emission are additionally marked with circles.

and VIRGO detectors (left-hand and centre panels, respectively) and the future advanced LIGO detector (right-hand panel), all for a distance to the source of 10 kpc. As a general feature, we note that the upper parts of these sensitivity diagrams are occupied by those models whose GW signal strength is enhanced by mode resonance. When mode resonance is not important, the largest characteristic amplitudes occur for those models which are most rapidly rotating, unless strong post-bounce damping is in action as in model CA1.

Both in Table 6 and in Fig. 24 the GW characteristics have been evaluated for a total emission time of $t_f = 50$ ms. In Appendix B we describe how to obtain the characteristic GW strain h_c for an *arbitrary* emission time using simple scaling laws.

6 CONCLUSION

In this paper, we have described numerical simulations of the phase-transition-induced collapse of rotating NSs to become hybrid quark stars. The simulations were made using a code which solves the general relativistic hydrodynamic equations in axisymmetry and within the conformally flat approximation. The initial stellar models were taken as being rapidly rotating $\gamma = 2$ polytropes, while during the evolution we used an EOS composed of three parts, depending on density: a normal hadronic-matter phase, a mixed phase of normal matter together with deconfined quark matter, and a pure quark matter phase. The hadronic component of the EOS was described with an ideal gas type of EOS, while for the deconfined quark matter phase we used the MIT bag model.

To validate our code, we first repeated several of the Newtonian simulations performed previously by LCCS. We found that the differential rotation which develops in these models during the post-bounce phase is almost entirely due to strong transient convection which arises because the way in which they treated the onset of the phase transition leads to an artificial negative specific-entropy gradient. We argue that their conclusion about there being a causal link between the large-amplitude post-bounce pulsations and the creation of differential rotation was a misinterpretation of the results. We also suggest that a significant part of the damping of the pulsations which they observed was a consequence of the numerical dissipation present in their calculations, rather than being related to differential rotation, although a part of this damping was related to the other physical processes which we have discussed here and which were present in both calculations.

Having clarified the dynamics of the collapse in the Newtonian framework, we then investigated the corresponding situation within GR, using a modified prescription for triggering the phase transition and initiating the collapse. Here we change the EOS only in the regions where the phase transition has taken place and leave it unchanged elsewhere. We recognize that our procedure for describing the phase transition remains extremely idealized but we believe that it represents a step forward.

Despite this difference in the way in which the phase transition is triggered, we have not found any major qualitative differences in the waveforms produced when comparing the relativistic simulations with the earlier Newtonian ones. Also in the general relativistic simulations, the waveforms produced are mainly composed of the fundamental $l = 0$ quasi-radial F mode and the fundamental $l = 2$ quadrupolar ^2f mode. However, in contrast to the Newtonian models, the F mode is at a lower frequency than the ^2f mode as a consequence of the different density profiles. In addition to these modes, a non-linear self-coupling of the F mode at twice the original frequency, the 2·F mode, is strongly excited due to the violent nature of the collapse. Although qualitatively similar to their Newtonian counterparts, the relativistic models exhibit quantitative differences in their dynamics. In order to investigate these, we have considered a set of 23 different models organized in several sequences. In each of these sequences, only one of the characteristic parameters of the models was allowed to vary.

The main trends observed were as follows. For the sequence with constant initial central rest-mass density, the maximum GW strain $|h|_{max}$ increases monotonically with the rotation rate (except for some models where the waveform is strongly altered by mode resonances). For the constant rest-mass sequence, on the other hand, we observe first an increase of $|h|_{max}$ with the rotation rate and then a decrease for very rapid rotation. For the sequence with constant rotation period but varying rest mass, we see $|h|_{max}$ increasing monotonically with the rest mass, which is a different behaviour from that seen for the Newtonian models, where $|h|_{max}$ first increases and then decreases again as the rest mass is increased. The reason

for this difference may simply be that having a decreasing part of the curve would require progenitor NSs with rest masses beyond the upper limit for general relativistic models. Finally, changing the EOS in the mixed phase has straightforward consequences: the central rest-mass density at bounce, the amplitude of the post-bounce oscillations, and the maximum GW strain all increase as the overall pressure in the mixed phase is reduced.

Other points to arise include the following. First, the influence of rotation on the frequencies of the F and ${}^2f$ modes agrees well with what was found by Dimmelmeier et al. (2006a) for pulsations of equilibrium NSs, suggesting that studies of linear pulsations of equilibrium models can (at least in some cases) correctly predict the properties of the eigenfrequencies also when the pulsations are excited in a dynamical situation. Secondly, in some models the emission of gravitational radiation is considerably enhanced by the non-linear resonance between the 2·F and ${}^2f$ modes. When the frequencies of these two modes are sufficiently close, the weakly radiating quasi-radial 2·F mode transfers some of its kinetic energy to the strongly radiating quadrupolar ${}^2f$ mode, leading to a considerable increase in $|h|_{\max}$. Thirdly, we have proposed a simple explanation for the strong damping of the post-bounce pulsations seen for a subset of our models. Our analysis reveals that that these models are all both rotating close to the Kepler limit and also undergoing large-amplitude post-bounce pulsations, resulting in significant mass shedding from the stellar surface close to the equator. As already discussed by Stergioulas et al. (2004), this ejection of loosely bound matter is very efficient in the damping quasi-radial pulsations.

In order to assess the prospects for the detection of phase-transition-induced collapse events by GW interferometers, special attention has been paid to making an accurate calculation of the GW emission resulting from this scenario. We find that the dimensionless GW strain h from a source at a distance of 10 Mpc ranges between 0.1 and 2.4×10^{-23} for all of the models considered and that the total energy emitted in GWs during first 50 ms of evolution is between 10^{-6} and $10^{-4}\,\mathrm{M}_\odot c^2$, corresponding to 2×10^{48} and 2×10^{50} erg, respectively. These numbers are considerably smaller than those presented by LCCS for their Newtonian calculations and so are disappointing for the prospects of detecting these sources. The damping times for the post-bounce oscillations, as computed from the gravitational radiation waveform, range from 8 to 687 ms for the F mode, and from 18 to 130 ms for the ${}^2f$ mode. For all of the models considered, we have also calculated the characteristic frequency f_c, the characteristic strain h_c, and the S/N for current and future detectors. For current detectors such as LIGO or VIRGO, all of the models (except one) have an S/N above 1 for a source at 10 kpc. For the advanced LIGO detector, the S/N rises to well above 10 for a source at 10 kpc for all of the models and reaches almost 400 when mode resonance is active. However, for detecting sources within the Virgo cluster at a distance of 20 Mpc, which is probably necessary in order to reach a realistic event rate, third generation detectors would be needed.

In conclusion, we note that while our study represents an improvement over previous ones, it still lacks a number of very important aspects which would be necessary for a properly realistic modelling of these objects. First, there is the treatment of the phase transformation itself which remains extremely crude, containing no detailed picture of the transformation of the material, the local heat input or the emission of neutrinos or photons. A consistent treatment of radiative transfer is likely to be essential for following the cooling phase of the newly formed hybrid quark star and could highlight that the radiative losses would produce differences in the specific-entropy stratification and hence trigger real convection. Also, in our discussion, we have been considering the phase transition as occurring by means of a detonation; the conclusions would be drastically altered if it takes place instead via a slow deflagration. A second aspect concerns the treatment of the standard neutron-star matter: while using a gamma-law EOS to model this can be reasonable for some simplified calculations, it gives an extremely poor approximation to the complex physics actually occurring in real NSs. Thirdly, we have not been considering the influence of magnetic fields which are not only expected to affect the dynamics, but could also lead to a dramatic modification of the phase transition process itself (Lugones et al. 2002). It is clear that future studies will need to take these aspects into account.

ACKNOWLEDGMENTS

It is a pleasure to thank Michal Bejger, Alessandro Drago, Kostas Glampedakis, Nikolaos Stergioulas, Shin Yoshida and J. Leszek Zdunik for helpful comments and discussions. We are grateful to Lap-Ming Lin for providing us with the reformulation of the source term for the energy equation, and to Marie Anne Bizouard for information about the scaling laws for the characteristic strain. Part of this work was done during a visit by EBA to the AEI in Golm, Germany, and a visit of HD to CAMK in Warsaw, Poland. We gratefully acknowledge the hospitality of the respective groups. This work was supported by DFG (SFB/TR 7) and by the DAAD and IKY (IKYDA German–Greek research travel grant). HD is a Marie Curie Intra-European Fellow within the 6th European Community Framework Programme (IEF 040464). The computations were performed at SISSA, AEI and MPA.

REFERENCES

Alcock C., Olinto A., 1988, Annu. Rev. Nucl. Part. Sci., 38, 161
Alford M., Blaschke D. B., Drago A., Klahn T., Pagliara G., 2007a, Nat, 445, E7
Alford M., Rajagopal K., Schaefer T., Schmitt A., 2007b, preprint (arXiv:0709.4635)
Alford M. G., Reddy S., 2003, Phys. Rev. D, 67, 074024
Andersson N., Kokkotas K. D., 1998, MNRAS, 299, 1059
Arnowitt R., Deser S., Misner C. W., 1962, in Witten L., ed., Gravitation: An Introduction to Current Research. Wiley, New York
Banyuls F., Font J. A., Ibáñez J. M., Martí J. M., Miralles J. A., 1997, ApJ, 476, 221
Benhar O., Ferrari V., Gualtieri L., 2004, Phys. Rev. D, 70, 124015
Benhar O., Ferrari V., Gualtieri L., Marassi S., 2007, Gen. Relativ. Gravit., 39, 9, 1323
Bhattacharyya A., Ghosh S. K., Joarder P. S., Mallick R., Raha S., 2006, Phys. Rev. C, 74, 065804
Bodmer A. R., 1971, Phys. Rev. D, 4, 1601
Burderi L., Possenti A., Colpi M., Di Salvo T., D'Amico N., 1999, ApJ, 519, 285
Cerdá-Durán P., Font J. A., Dimmelmeier H., 2007, A&A, 474, 169
DeGrand T., Jaffe R. L., Johnson K., Kiskis J., 1975, Phys. Rev. D, 12, 2060
Dimmelmeier H., Font J. A., Müller E., 2002a, A&A, 388, 917
Dimmelmeier H., Font J. A., Müller E., 2002b, A&A, 393, 523
Dimmelmeier H., Novak J., Font J. A., Ibáñez J. M., Müller E., 2005, Phys. Rev. D, 71, 064023
Dimmelmeier H., Stergioulas N., Font J. A., 2006a, MNRAS, 368, 1609
Dimmelmeier H., Cerdá-Durán P., Marek A., Faye G., 2006b, in Alimi J.-M., Füzfa A., eds, AIP Conf. Ser. Vol. 861, Albert Einstein Century International Conference. Am. Inst. Phys., Melville, p. 600
Dimmelmeier H., Ott C. D., Janka H.-T.Marek A., Müller E., 2007, Phys. Rev. Lett., 98, 251101

Donat R., Font J. A., Ibáñez J. M., Marquina A., 1996, J. Comput. Phys., 146, 58
Drago A., Lavagno A., Parenti I., 2007, ApJ, 659, 1519
Eardley D. M., 1983, in Deruelle N., Piran T., eds, Proceedings of the Advanced Study Institute, Les Houches, France, Gravitational Radiation. North-Holland Publishing Company, Amsterdam
Freire P. C. C., Wolszczan A., van den Berg M., Hessels J. W. T., 2008, ApJ, 679, 1433
Glendenning N. K., 1989, Phys. Rev. Lett., 63, 2629
Glendenning N. K., 1991, Nucl. Phys. B (Proc. Suppl.), 24B, 110
Glendenning N. K., 1992, Phys. Rev. D, 46, 1274
Glendenning N. K., 2000, Compact Stars. Nuclear Physics, Particle Physics, and General Relativity. Springer-Verlag, Berlin
Hagiwara K. et al. (Particle Data Group), 2002, Phys. Rev. D, 66, 010001
Horvath J. E., 2007, preprint (astro-ph/0703233)
Isenberg J. A., 1978, Waveless Approximation Theories of Gravities. University of Maryland Preprint (gr-qc/0702113)
Itoh N., 1970, Prog. Theor. Phys., 44, 291
Kokkotas K. D., Apostolatos T. A., Andersson N., 2001, MNRAS, 320, 307
Komatsu H., Eriguchi Y., Hachisu I., 1989, MNRAS, 237, 355 (KEH)
Lin L. M., Cheng K. S., Chu M. C., Suen W.-M, 2006, ApJ, 639, 382 (LCCS)
Lugones G., Ghezzi C. R., de Gouveia Dal Pino E. M., Horvath J. E., 2002, ApJ, 581, L101
Madsen J., 2000, Phys. Rev. Lett., 85, 10
Marranghello G. F., Vasconcellos C. A., de Freitas Pacheco J. A., 2002, Phys. Rev. D, 66, 064027
Miniutti G., Pons J. A., Berti E., Gualtieri L., Ferrari V., 2003, MNRAS, 338, 389
Nagar A., Zanotti O., Font J. A., Rezzolla L., 2007, Phys. Rev. D, 75, 044016
Ott C. D., Dimmelmeier H., Marek A., Janka H.-T., Zink B., Hawke I., Schnetter E., 2007, Class. Quantum Grav., 24, S139
Passamonti A., Bruni M., Gualtieri L., Sopuerta C. F., 2005, Phys. Rev. D, 71, 024022
Passamonti A., Stergioulas N., Nagar A., 2007, Phys. Rev. D, 75, 084038
Pfahl E., Rappaport S., Podsiadlowski P., 2003, ApJ, 597, 1036
Satz H., 1982, Phys. Lett. B, 113, 245
Shibata M., Sekiguchi Y.-I., 2003, Phys. Rev. D, 68, 104020
Shibata M., Sekiguchi Y.-I., 2004, Phys. Rev. D, 69, 084024
Shibata M., Sekiguchi Y.-I., 2005, Phys. Rev. D, 71, 024014
Stergioulas N., Friedman J. L., 1995, ApJ, 444, 306
Steffens F. M., Holtmann H., Thomas A. W., 1995, Phys. Lett. B, 358, 139
Stergioulas N., Apostolatos T. A., Font J. A., 2004, MNRAS, 352, 1089
Thorne K. S., 1980, Rev. Mod. Phys., 52, 299
Thorne K. S., 1987, in Hawking S. W., Israel W., eds, 300 Years of Gravitation. Cambridge Univ. Press, Cambridge
Weber F., 1999, Pulsars as Astrophysical Laboratories for Nuclear and Particle Physics. IOP Publishing, Bristol
Wilson J. R., Mathews J. R., Marronetti P., 1996, Phys. Rev. D, 54, 1317
Witten E., 1984, Phys. Rev. D, 30, 272
Zdunik J. L., Bejger M., Haensel P., Gourgoulhon E., 2007, A&A, 465, 533
Zdunik J. L., Bejger M., Haensel P., Gourgoulhon E., 2008, A&A, 479, 515

APPENDIX A: FINITE TIME FOR THE INITIAL PHASE TRANSFORMATION

In the study by LCCS, it was assumed that the time-scale of the phase transition is much smaller than the hydrodynamic time-scale for an NS, which is roughly 0.1 ms. They then ignored the finite velocity of the conversion process and instead induced the phase transition by instantaneously replacing the initial polytropic EOS by one including the quark matter, which gives a lower pressure.

However, since the time-scale for the phase transition even to two-flavour quark matter can be as long as 0.05 ms within our picture (which is comparable to the hydrodynamic time-scale), it is far from clear that treating it as instantaneous will not significantly affect the subsequent dynamics of the forming HQS. To check on this, we performed simulations for a set of representative collapse models in which we take the initial phase transformation to occur gradually over a finite time-scale with the values of $\rho_{\rm nm}$ and $\rho_{\rm qm}$ in equations (15) and (16) depending on the time t according to

$$\rho_{\rm hm}(t) = \begin{cases} \rho_{\rm c} - \frac{t}{\tau_{\rm conv}}(\rho_{\rm c} - \rho_{\rm hm}) & \text{for } t < \tau_{\rm conv}, \\ \rho_{\rm hm} & \text{for } t \geq \tau_{\rm conv}, \end{cases}$$
$$\rho_{\rm qm}(t) = \begin{cases} \rho_{\rm qm} + \rho_{\rm c} - \rho_{\rm hm} - \frac{t}{\tau_{\rm conv}}(\rho_{\rm c} - \rho_{\rm hm}) & \text{for } t < \tau_{\rm conv}, \\ \rho_{\rm qm} & \text{for } t \geq \tau_{\rm conv}, \end{cases} \quad \text{(A1)}$$

where $\tau_{\rm conv}$ is the time-scale of the initial phase transformation and $\rho_{\rm c}$ is the central rest-mass density. This means that $\rho_{\rm hm}(t)$ starts initially at $\rho_{\rm c}$ and then evolves linearly with time to reach its final value $\rho_{\rm hm}$ at $t = \tau_{\rm conv}$, while $\rho_{\rm qm}(t)$ has a similar behaviour shifted by $\rho_{\rm qm} - \rho_{\rm hm}$. For this test we set the time-scale equal to the approximate upper limit for a detonation type phase transition, $\tau_{\rm conv} = 0.05$ ms, and compared the results obtained with those for the regular models (corresponding to $\tau_{\rm conv} = 0$ ms).

We expected that having the initial phase transformation occurring gradually in this way would produce a time lag of the same order as $\tau_{\rm conv}$ in the initial contraction and give a less violent bounce occurring at a lower density with post-bounce pulsations of smaller amplitude than before. All of this was indeed the case for the models which we investigated, as can be seen in Fig. A1, where we show the time evolution of the central rest-mass density $\rho_{\rm c}$ for the representative model CA5 with $\tau_{\rm conv} = 0$ and 0.05 ms. The waveform of the emitted GWs remains essentially unaltered except for a small reduction in the first large-amplitude peaks and the expected phase shift (see Fig. A2). As the final HQS is less compact in the case of a non-instantaneous phase transition due to the less dynamic initial contraction, the frequencies of the predominantly excited quasi-normal modes, the F and ${}^2f$ modes, are modified only slightly, changing from 1.09 to 1.12 kHz and from 2.04 to 2.06 kHz, giving relative changes of 3–1 per cent, respectively (see Fig. A3).

The result that the differences seen when the finite $\tau_{\rm conv}$ is introduced are so small is a direct consequence of $\tau_{\rm conv} = 0.05$ ms still being about an order of magnitude smaller than the collapse time-scale in the case of an instantaneous initial phase transformation (although it is of the same order as the *dynamical* time-scale). The collapse time-scale can be approximated by the time of bounce, which is 0.40 ms for model CA5 and takes similar values for all of the other models. Since the choice $\tau_{\rm conv} = 0.05$ ms is an upper limit within our picture, we conclude that the taking $\tau_{\rm conv} = 0$ ms

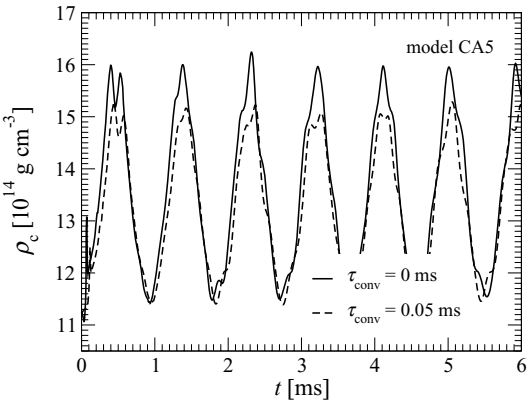

Figure A1. Time evolution of the central rest-mass density $\rho_{\rm c}$ for the GR collapse model CA5 with $\tau_{\rm conv} = 0$ ms (solid line) and $\tau_{\rm conv} = 0.05$ ms (dashed line).

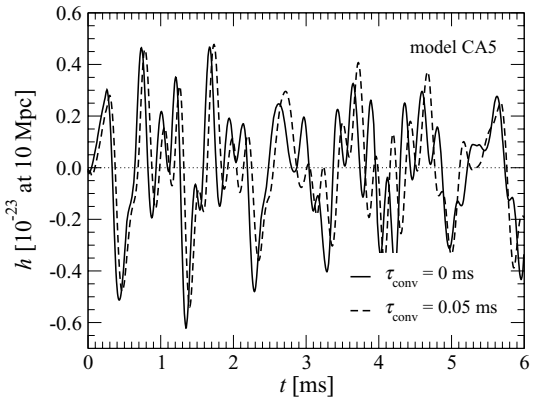

Figure A2. Time evolution of the GW strain h at a distance of 10 Mpc for the GR collapse model CA5 with $\tau_{\rm conv} = 0$ ms (solid line) and $\tau_{\rm conv} = 0.05$ ms (dashed line).

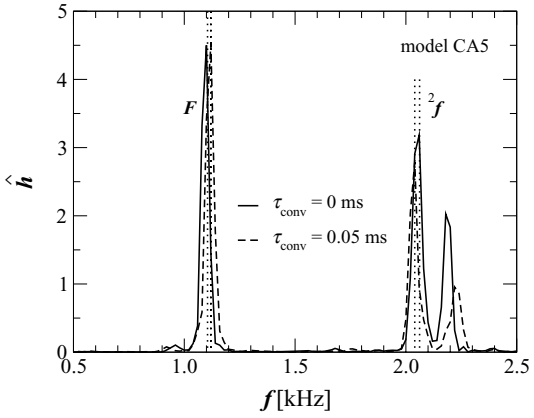

Figure A3. Power spectrum $\hat{h}$ (in arbitrary units) of the GW strain h for the GR collapse model CA5 with $\tau_{\rm conv} = 0$ ms (solid line) and $\tau_{\rm conv} = 0.05$ ms (dashed line).

for our regular collapse models was reasonable, giving values for quantities, such as $\rho_{\rm c,b}$, $|h|_{\rm max}$, $f_{\rm F}$ and $f_{^2{\rm f}}$ that are upper, but close, limits for a detonation type phase-transition-induced collapse of an NS to an HQS.

APPENDIX B: CALCULATION OF THE DAMPING TIMES OF THE WAVEFORMS

In order to determine the damping times for the GW emission we apply a curve fitting method to the numerically obtained waveform: the waveform is fitted by a series of damped sinusoids,

$$A_{20}^{\rm E2} = \sum_{i=0}^{n} A_i \, {\rm e}^{-t/\tau_i} \, \cos(2\pi f_i t + \phi_i). \tag{B1}$$

The parameters of this series (the damping times τ_i, the amplitudes A_i and the phases ϕ_i) are fixed by finding the best fitting curve. Depending on the model, we use $n = 4-5$ terms for the fitting procedure.

Note that this method of determining the damping times is more general than that presented in LCCS, where the series consisted of only two terms, so that only the fundamental $l = 0$ and 2 modes are taken into account, which leads to some inaccuracies at early post-bounce times when higher frequency modes in the GW signal are present. Also, they take $A_1 = A_2$ and $\phi_i = 0$, which may not be the case in general. With our approach we are able fit the original waveform with the correlation coefficient between the numerical data and equation (B1) exceeding 0.99 for all models, whereas the method used by LCCS gives a correlation coefficient of less than 0.9 for some models.

Assuming that the GW signal is essentially a linear combination of the F and ^2f modes, approximating each of them as a damped sinusoid and using knowledge of the mode frequencies $f_{\rm F}$ and $f_{^2{\rm f}}$, the amplitudes A_1 and A_2, and the phases ϕ_1 and ϕ_2, one can obtain the value of the characteristic GW strain $h_{\rm c}$ for an *arbitrary* emission time using simple scaling laws. For a single damped sinusoid,

$$h = h_0 \, {\rm e}^{-t/\tau} \sin(2\pi f t - \phi), \tag{B2}$$

where h_0 is the amplitude, τ is the damping time-scale, f is the frequency and ϕ is the phase. If $h_{\rm c}$ is known for some emission time $t_{\rm f}$, then its value for a multiple n of the original emission time can be calculated as

$$h_{\rm c}(n\, t_{\rm f}) = h_{\rm c}(t_{\rm f}) \sqrt{\frac{1 - {\rm e}^{-2nt_{\rm f}/\tau}}{1 - {\rm e}^{-2t_{\rm f}/\tau}}}, \tag{B3}$$

provided that $f^{-1} \ll \tau$ (which is fulfilled for most of our models) and the power spectral density S_h of the detector is reasonably constant in the vicinity of f. For an undamped sinusoid with $\tau = \infty$, equation (B3) gives $h_{\rm c}(n\, t_{\rm f}) = \sqrt{n}\, h_{\rm c}$ as expected; in other words, $h_{\rm c}$ scales like the square root of the number of cycles in the GW signal. In the limit of infinite emission time, but with finite τ, the exponential damping of the signal results in a finite value for the total characteristic GW strain,

$$h_{\rm c}(t = \infty) = h_{\rm c}(t_{\rm f}) \, \frac{1}{\sqrt{1 - {\rm e}^{-2t_{\rm f}/\tau}}}. \tag{B4}$$

For many of our models, we have F mode damping times $\tau_{\rm F}$ which are much longer than $t_{\rm f}$. On these time-scales, other damping mechanisms such as physical viscosity or GW back reaction (which are not taken into account in our study) could become important. We therefore do not give values of the total characteristic GW strain $h_{\rm c}(t = \infty)$ for our models.

This paper has been typeset from a TEX/LATEX file prepared by the author.